UNIVERSITÀ
DI PARMA

UNIVERSITÀ DEGLI STUDI DI PARMA

DOTTORATO DI RICERCA IN

"Scienza e Tecnologia dei Materiali"

CICLO XXXVIII

In-operando test of materials for thermomagnetic harvesting of low-grade waste heat

Coordinatore:

Chiar.mo Prof. Mauro Riccò

Tutore:

Chiar.mo Prof. Massimo Solzi

Dottorando:

Giovanni Garulli

ANNI ACCADEMICI 2022/2023 - 2024/2025

This work was funded by:

- **University of Parma** through the action Bando di Ateneo 2021 per la ricerca co-funded by MUR-Italian Ministry of Universities and Research - D.M. 737/2021 - PNR - PNRR – NextGenerationEU.
- **European Union** – NextGenerationEU under the National Recovery and Resilience Plan (NRRP), Mission 4 Component 2 Investment 1.1 - Call for tender No. 1409 of 14-09-2022 of Italian Ministry of University and Research (Project Code P2022KMXBL)
- **European Union** – NextGenerationEU, through the DM 351/2022 - PNRR – NextGenerationEU (Mission 4 Component 1).

"The hardest thing in the world is to change the minds of people who keep saying «But we've always done it this way»."

Grace Hopper

Contents

Chapter 1

Introduction

Harvesting low-grade waste heat from sources at temperatures below 100°C, which represents more than 60% of civil and industrial waste heat, and its conversion into mechanical or electrical energy represent a key goal for the transition to a green economy based on renewable energies and with a low human impact on the environment. In the last decade, many materials and different prototypes [1] [2] have been proposed for this type of applications. In this scenario, there is an emerging need for techniques able to characterize the materials' properties under realistic working conditions. However, materials performance is strictly connected to the thermomagnetic generators design, therefore a continuous process of device optimization is required along with material properties engineering. In this work, a laboratory-scale prototype of thermomagnetic generator is presented, designed for the rapid evaluation of thermomagnetic materials for energy-harvesting applications and for the test of different operational configurations [3]. The core of the device is a thermomagnetic motor, based on the Curie wheel principle, that converts thermal energy into mechanical energy and works between two temperature reservoirs, allowing the evaluation of materials performance on an adjustable temperature range. The motor shaft is connected to a custom-built, two-phase, miniaturized, permanent magnet electric generator specifically optimized for low-speed operation, which generates electric power and

enables the simultaneous measurement of torque, rotation speed and mechanical power output. The device can be operated with as low as 200 mg of active thermomagnetic material, allowing the use and characterization of candidate compounds even when only gram-scale batches can be obtained. The rotors are made, starting from powder of the thermomagnetic material and a plastic support, by means of a repeatable and easy-to-perform preparation method [2]. We report, as an example, the complete mechanical and electric power output evaluation of the prototype working with rotors based on different thermomagnetic alloys in the 20-60 °C temperature range. Thermal imaging technologies were employed to investigate thermal gradients in TM rotors during operation.

1.1 Thermomagnetic energy harvesting principles and devices

At present, thermoelectric conversion represents the predominant technology for the recovery of low-grade waste heat and its conversion to electric energy, but it is still characterized by low efficiencies and high costs [4][5]. Recently, interest has been rising in the scientific community for thermomagnetic generation, utilizing magnetic materials, as a promising alternative, particularly for harvesting of *low-grade* waste heat, i.e. released from sources at temperatures below the boiling point of water [4][5].

Many proof-of-concept prototypes of thermomagnetic generators (TMGs) have been developed, demonstrating the feasibility and potential of TM energy conversion in the context of low-grade waste heat harvesting[6][7], which can be grouped into three main categories[1]: thermomagnetic (rotary) motors (Fig. 1.1 a)[3][8][9], thermomagnetic oscillators (Fig. 1.1 b)[10] and static (inductive) thermomagnetic generators (Fig. 1.1 c)[11][12].

The working principle of this technology relies on thermomagnetic cycles, leveraging the temperature-dependent magnetization of a magnetic material. In the case of thermomagnetic motors (Fig. 1.1 a), which is also the

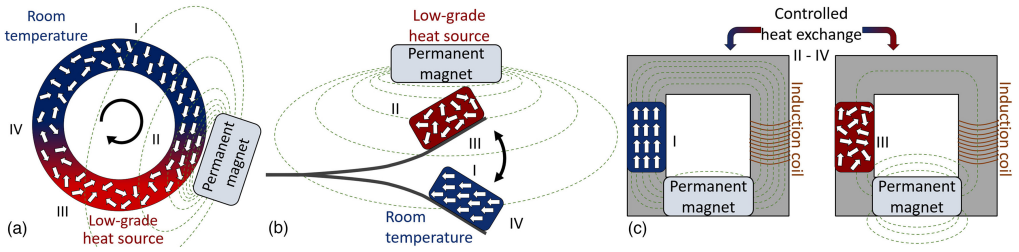

Figure 1.1: Sketches of (a) TM rotor, (b) TM oscillator and (c) TM static generator for the harvesting of waste heat. The TM material is colored in red or blue depending on its temperature. The arrows in the material depict the arrangement of magnetic moments inside the material. The numbers in brackets correspond to the steps of the TM cycle reported in Fig. 1.2. (From [3])

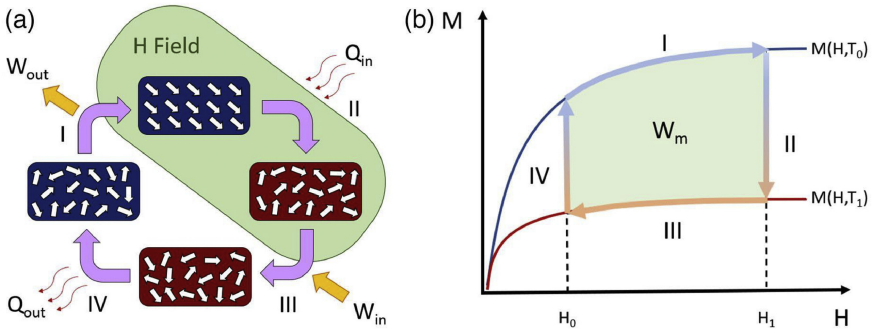

Figure 1.2: (a) Conceptual scheme of the thermomagnetic cycle exploited in TMGs and (b) representation of the cycle in the M-H diagram. The cycle is enclosed between two isotherm magnetization curves at temperatures T0 and T1. The useful magnetic work of the cycle Wm is highlighted by the green area. (From [3])

design analyzed and described with more detail in this work, the temperature dependency of the magnetization of the active material generates a gradient of attraction forces when the material itself is placed in a magnetic field gradient, thus producing a net torque and causing the rotation of the motor shaft; in this way, waste heat is converted by the TM motor into mechanical rotational energy, which can be in turn converted into electrical energy by connecting the TM motor shaft to a standard dynamo or alternator. Similarly, in thermomagnetic oscillators (Fig. 1.1b) the thermal energy causing the magnetization variation in the active material is converted into vibrational mechanical energy of a flexible cantilever on which the TM material is placed. The vibration movement of the cantilever itself also controls the cyclic thermal coupling between the TM material and the heat sources and therefore governs the TM cycle. The mechanical energy produced in this way can usually be converted into electric energy using a piezoelectric element[13] or inductively by means of a pickup coil positioned on the cantilever [10]. In the case of static thermomagnetic generators (Fig. 1.1c), valves are used to cyclically switch flows of hot and cold heat-transfer fluids through the TM material elements and the temperature-dependent magnetization change is exploited to induce a voltage in a pickup coil, achieving direct conversion of waste heat into electric energy.

A typical ideal thermomagnetic cycle involves two isothermal transformations, in which the magnetic field is applied (I) and removed (III), and two iso-field transformations, with the absorption of heat from a warm source (II) and its release to a cold source (IV). Both changes in temperature and field influence the magnetization of the material M(T,H), as depicted in Fig. 1.2b.

The concept was already proposed in the late nineteenth century by Nikola Tesla and Thomas A. Edison, who independently patented prototypes of thermomagnetic generators [14][15]. These devices, however, exhibited an extremely low efficiency and due to the use of iron as active magnetic material, characterized by a very high Curie temperature (Tc = 1043K), could

not be operated near room temperature. At such high temperatures other technologies proved to have higher efficiency and consequently the scientific community lost interest in thermomagnetic power generation. In recent decades, advancements in the study of magnetocaloric materials for magnetic refrigeration at room temperature [16], have sparked new interest in TM generation for low-grade heat harvesting [1][17], driven by the similarity in the desirable material properties for these two applications.

However, to fully develop the potential of thermomagnetic waste heat harvesting and make it economically sustainable and attractive for widespread use, we still need to identify high-performance, non-toxic, recyclable and cost-effective TM materials and perfect their integration into efficient devices.

Among the many desired properties, an effective TM material should exhibit a considerable magnetization change within the working temperature and field ranges of the target application. The satisfaction of this requirement relies on the selection of magnetic materials exhibiting a phase transition in the desired temperature range between two phases characterized by a significant difference in magnetization.

Additionally, it is necessary to consider the thermal characteristics of candidate TM materials: specific heat and thermal diffusivity govern the rate and the quantity of heat transferred between the material and the heat sources, influencing the useful work produced by the TM cycle and limiting the maximum working frequency of the generator, consequently limiting the maximum power output of the device [5][7].

Also, mechanical properties like machinability/formability and fatigue resistance play a key role in the production of the active elements to be integrated into TM devices and their long-time operational reliability.

Among the material families widely studied for magnetocaloric and thermomagnetic applications, MnFePSi and Heusler alloys represent broad classes of compounds exhibiting both first-order and second-order magnetic transitions with low thermal hysteresis and with critical temperatures that can be tuned over a wide range by varying the composition. These key characteris-

tics, combined with their low criticality in terms of raw materials availability and their low toxicity, make them highly promising materials for TM low-grade waste heat harvesting [1].

A third promising category of candidate materials, already investigated for magnetocaloric applications [17] but yet not deeply evaluated for TM energy conversion and harvesting, is represented by FeBZr-based amorphous alloys, because they exhibit a soft ferromagnetic behavior, with a high saturation magnetization and a Curie temperature tunable by variation of the alloy iron content [18]. They are also constituted by abundant, non-toxic and non-critical elements and can be easily produced by melt spinning technique, making the production process industrially scalable and potentially low-cost. It is alto worth mentioning that the use of melt spinning as a preparation technique produces thin metallic ribbons, making these materials ideal candidates for the manufacturing of rotors to be integrated in *Curie wheel* thermomagnetic motors.

Chapter 2

TMG Device design and characterization

2.1 Thermomagnetic motor design

The chosen design for the thermomagnetic harvester prototype is the *Curie Wheel* type of thermomagnetic generator.
The core of the device is a ring, made of a composite containing the active thermomagnetic material under test, fixed on a shaft that is free to rotate. For all the cases evaluated in this work, a ferro- to paramagnetic transition in the material is exploited, but also other types of magnetic phase transition involving a change in magnetization can be used.
In our implementation of the *Curie Wheel* (schematic in fig. 2.1), an electric resistor is used to simulate a source of waste heat. A small pool of water provides enhanced thermal contact between the heater and the thermomagnetic rotor, while a thermocouple allows measurement and control of the temperature of the hot side of the machine. The upper part of the wheel instead is exposed to the ambient air and allowed to cool down. If the critical temperature of the active material is between the room temperature and the hot side temperature of the device, we can expect the cold part of the rotor to be ferromagnetic and the hot part to become paramagnetic.

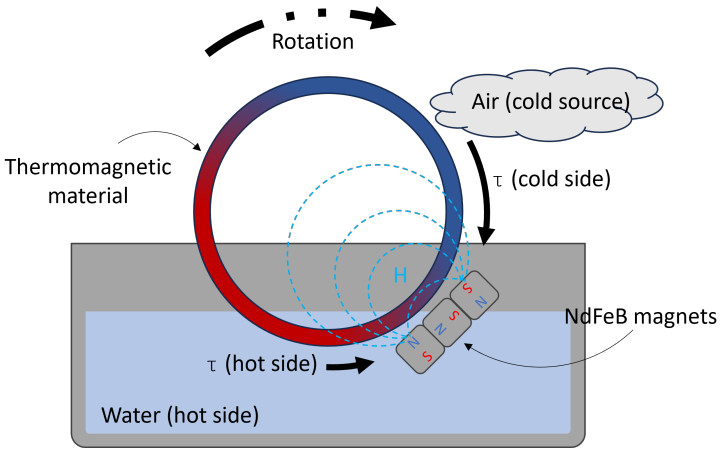

Figure 2.1: Thermomagnetic generator schematic and working principle.

The thermomagnetic rotor is placed in a magnetic field gradient, generated by three Nd-Fe-B magnets, arranged as a single element of a Halbach array to maximize field intensity near the wheel. The magnetic field gradient generated by the magnets magnetizes the wheel segment close to the magnets, but the magnetization is higher on the cold ferromagnetic side of the wheel than on the hot paramagnetic side. Since the wheel is placed in the magnetic field gradient, the cold portion of the wheel experiences a stronger attraction force to the magnets and a net torque is produced on the shaft; this torque causes the shaft to rotate and the cold part of the wheel to enter the hot water and transition to the paramagnetic state. The thermomagnetic cycle is finally closed when the material emerges from the hot water far away from the magnet and is exposed to the ambient air, therefore being allowed to cool down and transition to the ferromagnetic phase.
In this way, a continuous rotation of the shaft is produced and the generated mechanical energy can be converted to electric energy by coupling the device shaft to an electric generator.

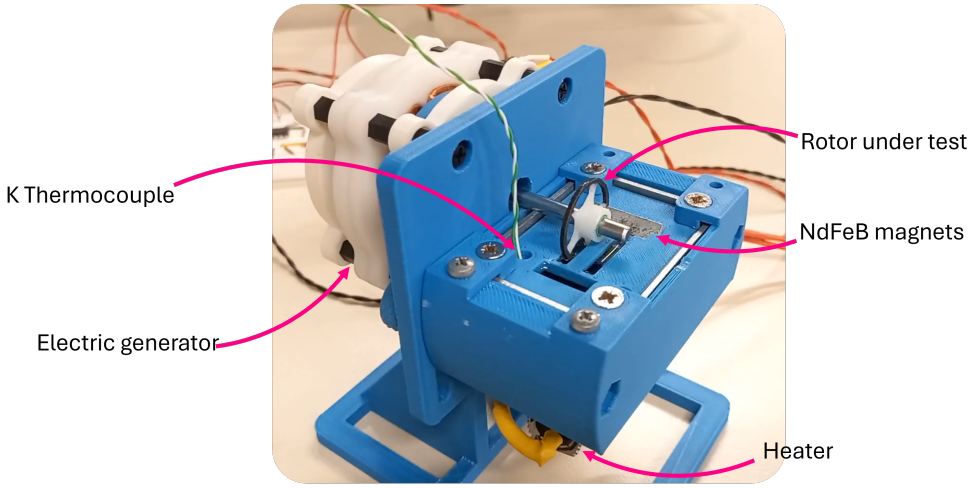

Figure 2.2: Thermomagnetic generator prototype used to test thermomagnetic materials.

2.2 Electric generator design

To convert the generated mechanical power into electric energy, a permanent magnet, iron-less core generator design was chosen to minimize detent torque and losses in the stator core.

To make the generator more compact and easier to manufacture, an axial-flux generator topology was employed, with a rotor composed by two discs, each containing 8 arc-shaped Nd-Fe-B magnets with opposite polarities oriented along the shaft direction.

To achieve constant torque and consequently constant power while running at constant speed, a two-phase winding design was implemented. Each of the two identical windings is composed by 8 coils of 1000 turns each of self-bonding magnet wire of 0.017mm nominal diameter. The windings are of the same shape and mounted overlapping, placed between the two rotor discs carrying the magnets (see fig. 2.3). The two windings are shifted of 22.5° and as a result the two produced electric signals are out of phase of 90 electrical degrees.

Each coil was wound separately on specifically shaped 3D-printed spindle. The coils were then heated to a temperature of 130°C via joule heating for

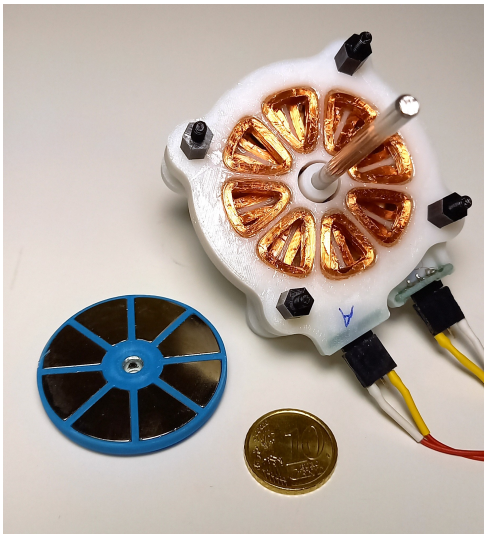

Figure 2.3: Partial assembly of the two-phase generator rotor (left) and stator (right).

10 minutes to activate the self-bonding coating of the copper wire. The actual temperature of the winding was estimated in real time during the baking process by measuring voltage and current provided to heat the winding wire. All the process was controlled from a PC running a Matlab script implementing a PID algorithm to stabilize the temperature and automatically control baking time. Finally, all the coils were glued in place in the generator stator and connected in series.

For a permanent magnet electric generator, we can define the *velocity constant* as the ratio between rotational speed and peak output voltage under no-load conditions:

$$K_v \equiv \frac{\omega}{V_{peak(no-load)}} \tag{2.1}$$

For the two-phase generator design and assuming that both windings have the same Kv value and zero internal resistance and neglecting higher order harmonics, we can describe the voltage output of the generator in the time domain as:

$$\begin{aligned} V_{A(ideal)}(t) &= V_{peak(no-load)A} \cdot sin(N\omega t + \phi) = \frac{\omega}{K_v} \cdot sin(N\omega t + \phi) \\ V_{B(ideal)}(t) &= V_{peak(no-load)B} \cdot cos(N\omega t + \phi) = \frac{\omega}{K_v} \cdot cos(N\omega t + \phi) \end{aligned} \tag{2.2}$$

Equation (2.2) can be modified to predict the real generator voltage output at the load taking into account a different Kv value for each winding and the voltage drop on the internal resistance of the winding as well:

$$\begin{aligned} V_{loadA} &= V_{A(ideal)}(t) - I_{loadA}(t) \cdot R_{intA} = \frac{\omega}{K_{vA}} \cdot sin(N\omega t + \phi) - I_{loadA}(t) \cdot R_{intA} \\ V_{loadB} &= V_{B(ideal)}(t) - I_{loadB}(t) \cdot R_{intB} = \frac{\omega}{K_{vB}} \cdot cos(N\omega t + \phi) - I_{loadB}(t) \cdot R_{intB} \end{aligned} \tag{2.3}$$

By rearranging the terms, we obtain:

$$\begin{aligned} \frac{\omega}{K_{vA}} \cdot sin(N\omega t + \phi) &= V_{loadA} + I_{loadA}(t) \cdot R_{intA} \\ \frac{\omega}{K_{vB}} \cdot cos(N\omega t + \phi) &= V_{loadB} + I_{loadB}(t) \cdot R_{intB} \end{aligned} \tag{2.4}$$

Taking the sum of the square of each member of the last two equations, we derive:

$$\begin{aligned} &\omega^2(sin^2(N\omega t + \phi) + cos^2(N\omega t + \phi)) = \\ &\quad K_{vA}^2(V_{loadA} + I_{loadA}(t) \cdot R_{intA})^2 + K_{vB}^2(V_{loadB} + I_{loadB}(t) \cdot R_{intB})^2 \end{aligned} \tag{2.5}$$

This allows us to directly estimate the instant shaft rotational speed of the generator by measuring voltage and current output at the electric load for both windings, assuming the velocity constant K_v and the internal resistance R_{int} are known for each winding:

$$\omega(t) = \sqrt{K_{vA}^2(V_{loadA}(t) + I_{loadA}(t) \cdot R_{intA})^2 + K_{vB}^2(V_{loadB}(t) + I_{loadB}(t) \cdot R_{intB})^2} \tag{2.6}$$

A similar relation holds for torque and armature current:

$$\tau(t) = \sqrt{K_{\tau A}^2 I_{loadA}(t)^2 + K_{\tau B}^2 I_{loadB}(t)^2} \tag{2.7}$$

where $K_{\tau A}$ and $K_{\tau B}$ are the motor torque constant for armatures A and B respectively. When all the quantities are expressed in SI units, the torque constant of this type of motor equals the inverse of the motor velocity constant:

$$K_\tau = \frac{1}{K_v} \tag{2.8}$$

In this way, torque on the generator shaft can be estimated by means of measuring the armature current on both windings:

$$\tau(t) = \sqrt{\frac{1}{K_{vA}^2} I_{loadA}(t)^2 + \frac{1}{K_{vB}^2} I_{loadB}(t)^2} \tag{2.9}$$

Once torque and angular speed have been estimated, their product gives the estimate of mechanical power output:

$$P(t) = \tau(t) \cdot \omega(t) \tag{2.10}$$

2.3 Measurement control and data acquisition

To measure the mechanical power and torque output of the device at different rotational speed regimes, a programmable electronic load was designed to be connected to the electric generator output; the resistance value of the load connected to the generator sets the ratio between voltage output and current, but since voltage output is proportional to the rotation speed and armature current is proportional to torque, changing the load resistance value has the effect of changing the generator torque-to-speed ratio; when the device is operational and the thermomagnetic rotor is rotating the shaft, this indirectly changes the running speed of the device.

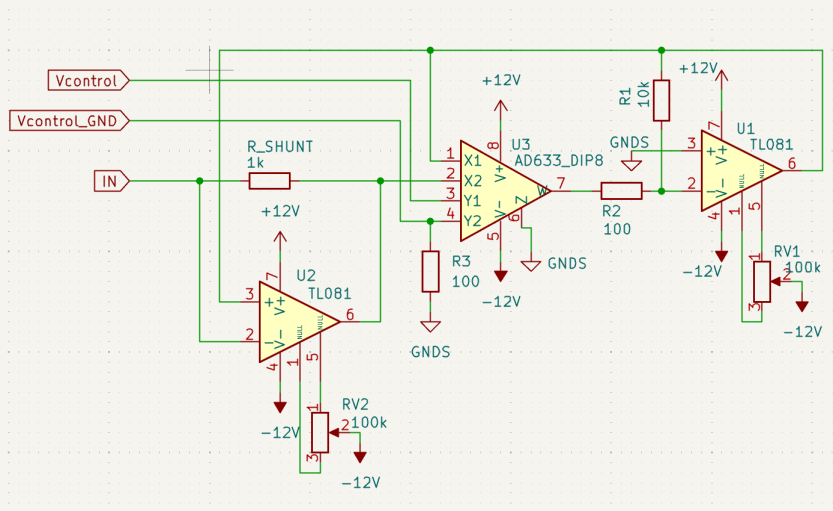

Figure 2.4: Schematic of the electronic load used to control the thermomagnetic generator prototype.

The designed circuit, represented in fig. (2.4), is essentially an impedance converter modified by introducing the 4-quadrant analog multiplier AD633 to allow the gain of the circuit to be changed by an external control voltage provided by an analog output channel of a data acquisition card. This circuit, when connecting an electric signal between the IN terminal and ground, behaves as a resistor of value proportional to the control voltage:

$$R_{load} = -\frac{R_1}{R_2} \cdot R_{shunt} \frac{V_{control}}{10V} \tag{2.11}$$

While the device is running, the same data acquisition card used to control the electronic load was used to record voltage output of the generator and the potential difference across the shunt resistor R_{shunt}, which allows to calculate armature current.

2.4 Device calibration

To calibrate the electric generator to allow measurement of speed and torque, a specific procedure was carried out to experimentally determine the velocity

constant of the generator, the winding internal resistance and the friction torque due to the ball bearings supporting the generator shaft.
To get a first estimate of the Kv, the generator windings were connected to a two-channel oscilloscope; the shaft was hand-spun and the oscilloscope used to measure the signal frequency, equivalent to 4 times she shaft rotation frequency, and the peak voltage output in nearly no-load conditions.
Then multiple measurements were carried out at variable electric loads while attaching to the shaft a pulley wound by a thin cotton wire carrying a calibrated weight. With this setup, when constant speed is achieved we can assume a constant torque on the shaft equivalent to the product between g, the mass of the calibrated weight and the radius of the pulley.

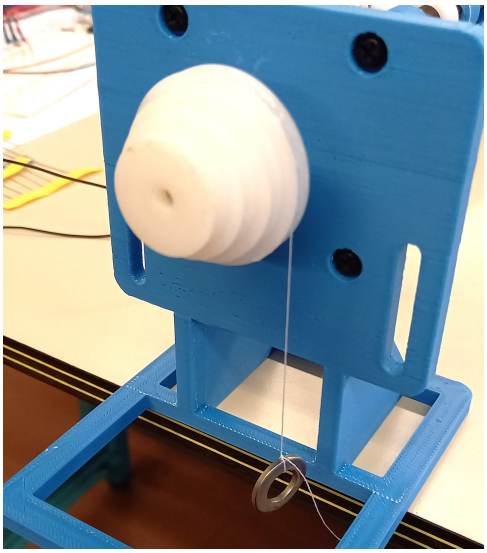

Figure 2.5: Setup used for calibrating generator construction parameters.

The voltage output of the generator, once corrected for the voltage drop on the internal resistance of the windings, is directly proportional to rotation speed and allows to accurately estimate the Kv of the generator. Both frequency and amplitude of the electric output were obtained through best fit of the signal data using a one-term fourier function.
The expected torque on the shaft is then computed from armature current and the estimated Kv. The difference between the true known *true* torque

generated by the calibration pulley and the torque estimated from the current is assumed to be due to friction in the bearings, plotted against ω and modelized with a 1st order polynomial fit.

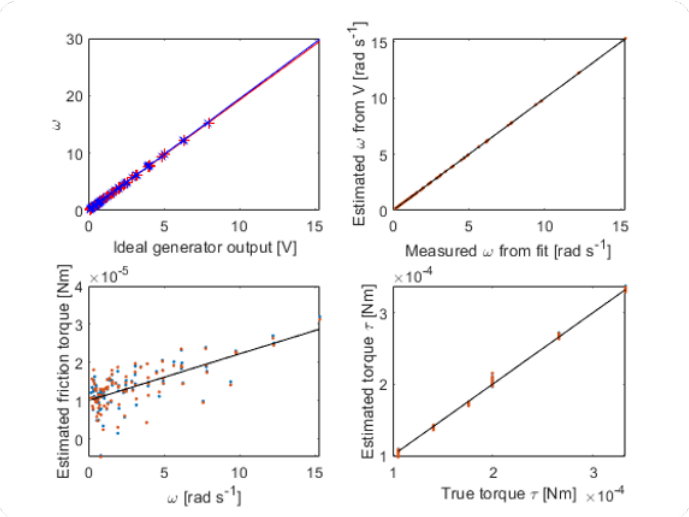

Figure 2.6: Validation of the calibration process by comparing *true* known values of torque and speed to the values estimated by voltage and current output.

2.5 Thermomagnetic rotor fabrication process

To test and use thermomagnetic materials in energy harvesting applications, there is the need for techniques to shape the materials into the active components required in the device to be designed. Since materials of interest for this field usually exhibit poor mechanical properties and are not easily machinable, one of the possible solutions to this problem is grinding the material to powders and embedding the powder grains in an epoxy matrix, obtaining composite materials; the use of epoxy allows the use of molds to cast pieces of the required shape and the epoxy matrix can be enriched with additional materials to improve thermal conduction[2].

To allow to test multiple different materials in the thermomagnetic harvester prototype, a new reliable, repeatable and easy to perform method was devel-

oped to cast epoxy-based composite materials into ring shaped thermomagnetic rotors (fig. 2.7).

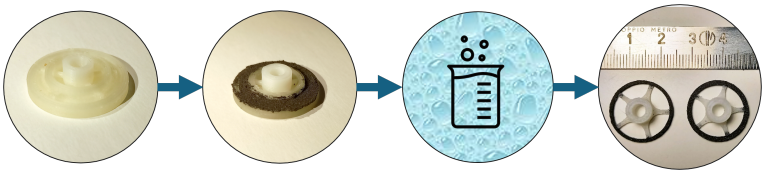

Figure 2.7: Steps of the process used to produce epoxy-based composite thermomagnetic rotors.

This method relies on the use of molds produced using a dual-extruder 3D printer, allowing possibly to obtain rotors of different sizes and shapes. The mold itself is printed using BVOH (butenediol vinyl alcohol copolymer), a water-soluble biopolymer. At the same time, a support for connecting the active rotor to the TM motor shaft is printed, embedded in the mold, using regular ABS plastic (acrylonitrile butadiene styrene). The support is specially designed to minimize contact area with the active material and enhance the heat exchange of the rotor with the environment.
To produce a thermomagnetic rotor, a weighed amount of powders of the materials to be tested is first mixed with a weighed amount of epoxy. The composite is transferred to the mold while the epoxy is fresh and may undergo a curing process if needed. Once the epoxy has hardened, warm water is used to dissolve the mold, leaving the active thermomagnetic rotor already mounted on the ABS support. This has also the benefit of allowing to gently free the rotor from the mold without applying mechanical stress to the composite parts.
In our case, for the fabrication of all the composite-based rotors, a commercial vinyl ester epoxy was used (Distitron VE 100 by Polynt) in an amount corresponding to 24% of the mass of the powder; this quantity was empirically found to be the minimum amount required to successfully bind the powder grains: higher fractions would degrade performance in the device because of the lower density of active material.

Finally, each rotor underwent a curing phase at 60°C for 4 hours to improve the hardening of the epoxy matrix.

2.6 Temperature controller design

Since regular PWM driving of the heater in the device was found to produce EMI interference in the analog circuitry connected to the electric generator, an Arduino-based circuit was designed implementing a more sophisticated PID controller. The controller measures the water bath temperature using a thermocouple and trough a proportional-integral-derivative algorithm controls the electric power fed to the resistive heater in the harvester prototype. To minimize EMI emission without compromising efficiency, instead of directly driving the heater in on-off mode, a power output stage featuring a buck topology converter was included in the controller design and driven by the Arduino microcontroller using PWM. A second thermocouple module connected to the controller allows to measure also the ambient temperature. The temperature controller can be connected to a computer via USB and interrogated using SCPI commands, allowing for automatization of the data acquisition.

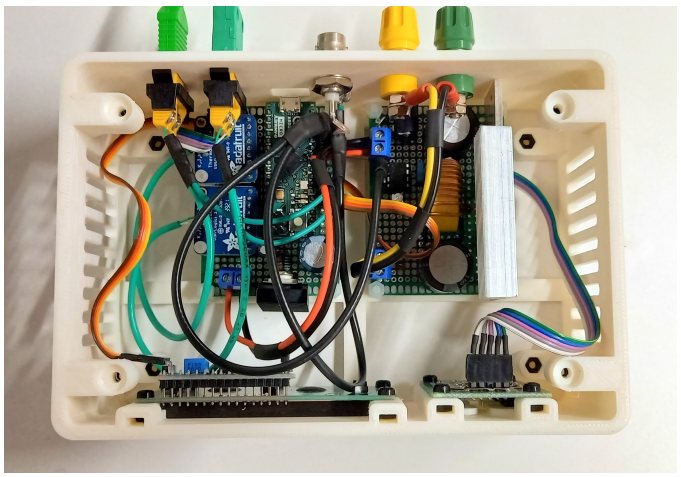

Figure 2.8: Temperature controller assembly.

Chapter 3

Heusler Alloys

3.1 Experimental

Three Heusler alloys, with nominal compositions $Ni_{48}Mn_{36}Sn_{16}$, $Ni_{48}Mn_{36}In_{16}$, and $Ni_{50}Mn_{19}Cu_6Ga_{25}$, were synthetized by arc melting under Ar atmosphere the stoichiometric amount of high-purity (99,99%) elements. To compensate for evaporation losses, a 1% excess of Mn was added. The ingots were flipped and re-melted three times to improve homogeneity. The samples were annealed at 1073 K for 72 hours and then quenched into water. The composition of the samples was analysed using energy dispersive X-ray spectroscopy (EDX) in a scanning electron microscope (Bruker Esprit microanalysis on a FEG-ESEM FEI QUANTA 250). All samples compositions were found to be in agreement with the nominal ones within the 1% margin of experimental error. The prepared bulk samples were manually ground in an agate mortar and sieved to obtain powders with a maximum grain size of 120µm. The powders were annealed at 773 K for 4 h in Ar atmosphere, followed by slow cooling, to reduce the stresses introduced during the grinding process and to recover the magnetic properties of the bulk samples [19] [20].
The temperature dependence of the low-field a.c. magnetic susceptibility of the samples was measured as a function of temperature with an applied ac magnetic field of 1 mT using a ThermoMagnetic Analyzer (TMA). This

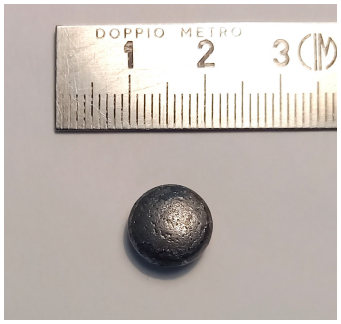

Figure 3.1: NiMnIn ingot obtained by arc melting.

allowed to identify the Curie temperature of the materials and confirm the absence of other magnetic transitions. Magnetization measurements were performed as a function of temperature using an extraction magnetometer (Maglab2000 System by Oxford Instruments) and a force magnetometer (DSM8 by Manics). These measurements were used to obtain high-field magnetization values and to calculate the potential thermomagnetic performance of the materials from M(T,H) data.

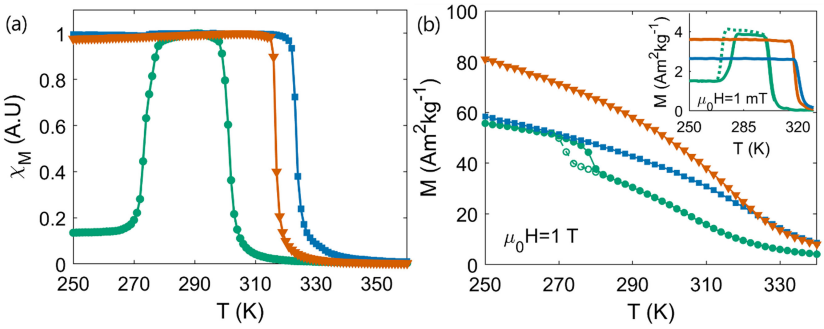

Figure 3.2: (a) normalized ac magnetic susceptibility in zero applied dc magnetic field and (b) magnetization in 1T applied magnetic field as a function of temperature for the alloys: $Ni_{48}Mn_{36}Sn_{16}$ (blue squares), $Ni_{48}Mn_{36}In_{16}$ (orange triangles), and $Ni_{50}Mn_{19}Cu_6Ga_{25}$ (green circles). Inset of (b): magnetization of the three samples in an applied magnetic field of 1 mT [3].

For this study, ring-shaped rotors were prepared for each of the three investigated materials (NiMnIn, NiMnSn and NiMnCuGa) following the procedure described in section 2.5. The fabricated rotors have an external diameter

of 20 mm, an internal diameter of 18 or 17 mm and a length of 1 mm (fig. 3.3). Utilizing a composite with 87±2 wt% magnetic powder, the net mass of active magnetic material in the rotors with an internal diameter of 18 and 17 mm is approximately 0.23±0.01 g and 0.34±0.01 g, respectively.

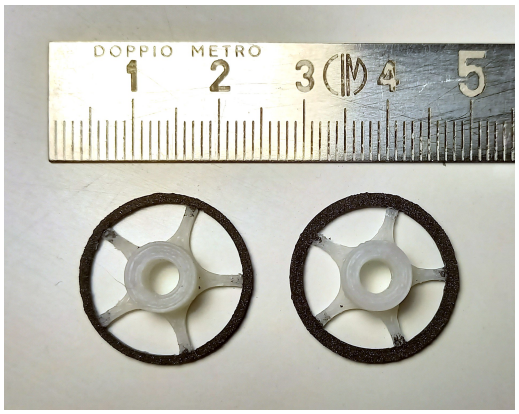

Figure 3.3: Example of rotors made of NiMnIn with a radial thickness of 1 mm and 1.5 mm[3].

The evaluation of the three materials in the TM motor was performed recording mechanical power output and rotation speed while varying the resistive load and the temperature of the hot water. The load sweep was conducted in both increasing and decreasing load resistance to verify measurement repeatability. Power versus speed curves were recorded for each rotor by using as cold source a controlled forced flow of thermostated air at 297 K and with increasing warm water temperatures in 5 K increments from 303 K to 338 K. The rotor was submerged to a depth of 3 mm in the water. This level was selected to position the peak of the stray magnetic field at the water surface. Consequently, one peak of the magnetic field gradient is situated just above the water level, while the other peak is fully immersed in the warm water. Under static conditions, this geometrical configuration of the TM motor maximizes the torque on the rotor by optimizing the temperature difference between the sections experiencing the maximum field gradient.
More experiments were performed to estimate the real working temperatures of the active material by infrared thermography analysis while operating the

device on natural air convection for cooling.

3.2 Results and discussion

3.2.1 In operando evaluation for TMG

Figures 3.4, 3.5, 3.6 report the mechanical power output as a function of the angular speed for the three materials at different values of T1, while maintaining the cold side temperature constant at 297 K. Generally, the power output increases as the temperature of the warm heat source increases, owing to the enlargement of the cycle area and of the magnetization change during the thermomagnetic cycle. However, this trend varies with the rotation speed. Under a heavy external load, the rotation speed is low while torque saturates, limiting the power output. As the electric load decreases, the rotational speed increases, leading to an increase of the power output to a maximum value. With a further increase in speed, we observe a stabilization or even a decrease in power output, especially for measurements performed with T1 exceeding the Curie temperature of the exploited material. This effect is caused by the reduction of the real thermal span experienced by the material when increasing rotational speed. This results in a decrease in the magnetization variation during the cycle and, consequently, in the output power. When the mean temperature of the cycle surpasses the Curie temperature of the active TM material, the reduction in dM/dT induces a decrease in the net torque of the rotor and, consequently, in the power output. This effect is more pronounced for NiMnCuGa (fig. 3.6), which has the lowest Curie temperature in the series.

Figure 3.7 compares the maximum power output as a function of T1 for the three materials. NiMnCuGa, having the lowest T_c among the three samples, produces the maximum output at low temperatures. As the warm reservoir temperature increases, the NiMnCuGa output tends to stabilize, whereas the output of NiMnIn and NiMnSn increases. The NiMnIn alloy shows a maximum mechanical output of 0.70±0.04 mW, which corresponds to 3.0±0.1

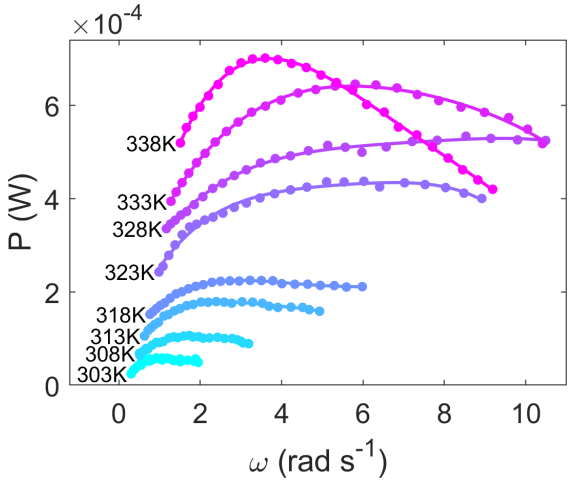

Figure 3.4: Mechanical power output of the TM motor prototype as a function of the shaft speed obtained by varying the temperature of the warm source (T1) and the external resistive load exploiting rings of NiMnIn. Each point represents the average between the measurements performed with increasing and decreasing load sweep. The solid lines are the polynomial interpolation of experimental data[3].

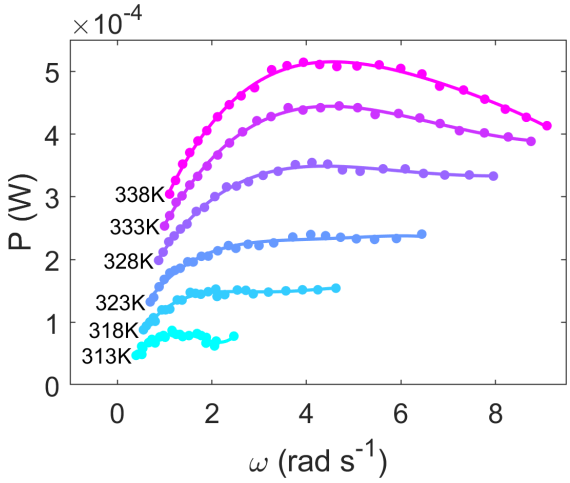

Figure 3.5: Mechanical power output of the TM motor prototype as a function of the shaft speed obtained by varying the temperature of the warm source (T1) and the external resistive load exploiting rings of NiMnSn. Each point represents the average between the measurements performed with increasing and decreasing load sweep. The solid lines are the polynomial interpolation of experimental data[3].

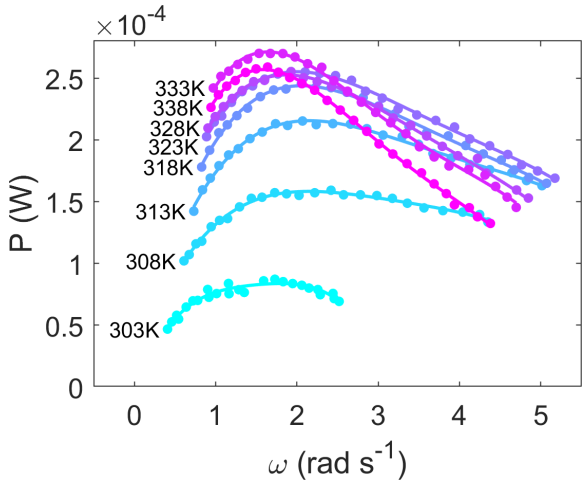

Figure 3.6: Mechanical power output of the TM motor prototype as a function of the shaft speed obtained by varying the temperature of the warm source (T1) and the external resistive load exploiting rings of NiMnCuGa. Each point represents the average between the measurements performed with increasing and decreasing load sweep. The solid lines are the polynomial interpolation of experimental data[3].

W/kg or 23.7±0.4 mW/cm3, considering the output power normalized to the mass or to the volume of the active material.

To further investigate the mechanisms leading to a power output drop associated to increased rotational speed, additional experiments were performed to compare the output of 3 rotors made by the same NiMnIn material: a ring rotor with a radial thickness of 1 mm (internal diameter of 18 mm), a ring rotor with a radial thickness of 1.5 mm (internal diameter of 17 mm) and a tandem-rotor made of 2 rings with a radial thickness of 1 mm on the same shaft (fig. 3.8).

The three rotors contain 0.23 ± 0.01 g, 0.34 ± 0.01 g and 0.46 ± 0.02 g of the active TM material, respectively. The distance between the two rings in the tandem-rotor, set at 6 mm, proved to be sufficient to treat the two rotors as independent thermal bodies and avoid any effects related to water capillarity. The power output of the tandem rotor is approximately double of the single 1 mm rotor, resulting in a mass-normalized power output of 3.0 ± 0.1 W/kg

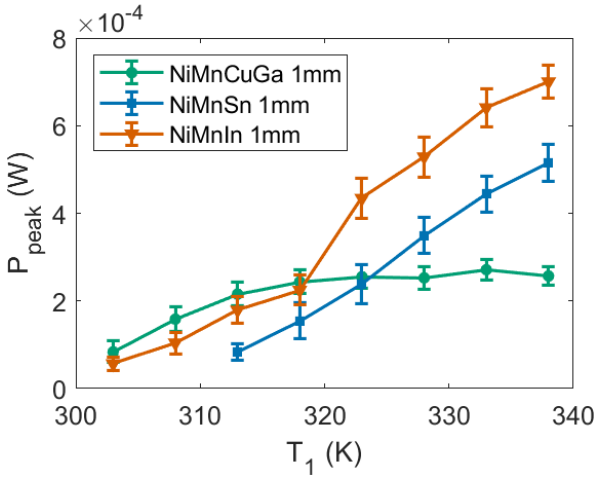

Figure 3.7: Maximum mechanical power output as a function of temperature of the warm reservoir for a rings of 1 mm thickness of NiMnIn (orange triangles), NiMnSn (blue squares) and NiMnCuGa (green circles). Solid lines serve as guide to the eyes[3].

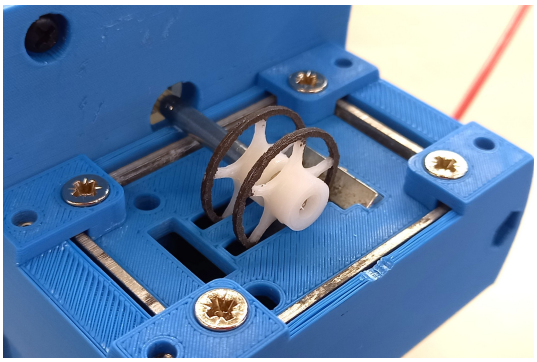

Figure 3.8: Thermomagnetic generator prototype operation using a *tandem* NiMnIn rotor.

at a hot side temperature of 338 K. On the opposite, the thickest rotor does not show an increase of the power output proportional to the mass of active magnetic material: its normalized power is limited to 2.4 ± 0.1 W/kg (fig. 3.9)

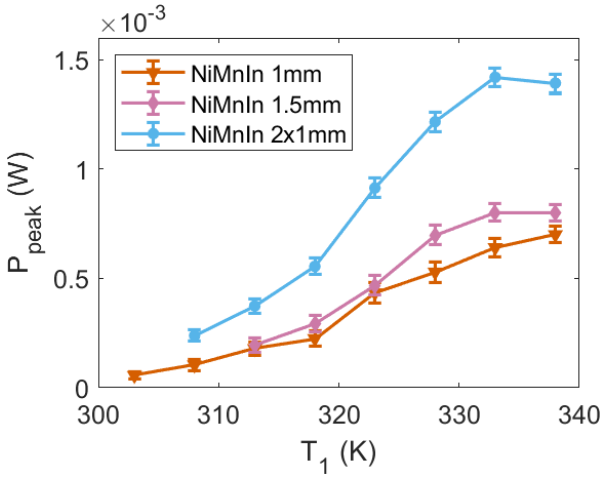

Figure 3.9: Comparison of the maximum mechanical power output as a function of temperature of the warm reservoir for: a single ring of NiMnIn with a radial thickness of 1 mm (orange triangles), a single ring of NiMnIn with a radial thickness of 1.5 mm (pink diamonds) and two rings of NiMnIn with a radial thickness of 1 mm fixed to the same shaft (azure circles). Solid lines serve as guide to the eyes[3].

This limitation can be attributed to the heat transfer between the rotor and the environment and may signify that the inner parts of the TM materials are contributing less to the mechanical power output than the outer shell. This result also suggests that the heat exchange rate at the interface between the rotor and the fluid (air or water) is currently the limiting factor of the power output of the TM motor. Enhancing heat exchange at the interface and increasing the surface-to-volume ratio of the active rotor are then critical objectives for further improving the power and efficiency of TMGs.

3.2.2 Infrared thermography

To further investigate the role of heat exchange rates in the TMG device, it is imperative to determine the effective temperatures reached by the active material during the thermomagnetic cycle and how they vary throughout rotation.

A preliminary result of infrared (IR) thermography analysis of the rotor during operation is shown in figure 3.10. The thermal image was acquired using a high-resolution infrared camera (FLIR SC7000) while the TM motor, equipped with the 1 mm thick NiMnIn rotor, operated with the warm source temperature set to 323 K and a rotational speed of 1.5 rad/s. The thermal image of the TM motor and the analysis of the angular temperature distribution in the rotor reveal a thermal gradient in the portion of the rotor outside the water. A total temperature difference of about 6.5 K is observed, with the maximum temperature being 5 K lower than the water temperature and the minimum temperature of the cycle being about 14 K higher than room temperature. This preliminary thermal analysis confirms that the temperature difference experienced by the material within the cycle is lower than the difference between the thermal sources, and the maximum temperature reached by the material is lower than the temperature of the warm source.

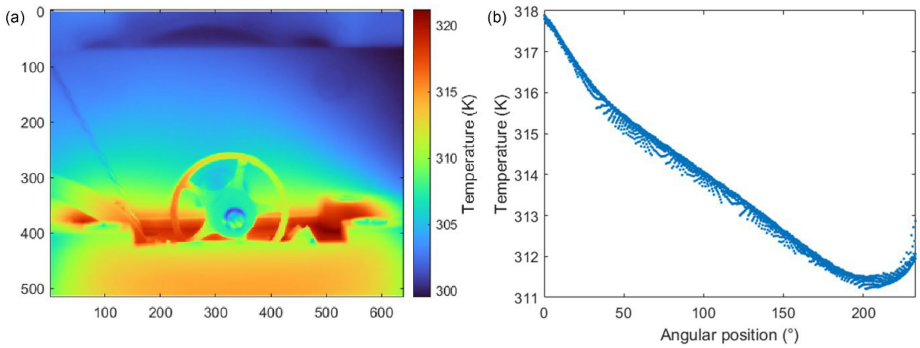

Figure 3.10: (a) Infrared thermal image of the exposed parts of the thermomagnetic motor during operation, equipped with the 1 mm thick NiMnIn rotor. The warm heat source is maintained at 323 K. The load is adjusted to achieve a rotational speed of approximately 1.5 rad/s. (b) Temperature of the angular segments of the rotor above the warm water as a function of angular position starting from the water surface on the left[3].

Chapter 4

FeBZr amorphous alloys

In collaboration with University of Sevilla (ES)

A series of four FeBZr samples was produced, with the aim of testing new materials of potential interest for low-grade waste heat energy harvesting applications. For this kind of employ, some key characteristics of a candidate material would be a high saturation magnetization, a magnetic transition temperature near room temperature tunable by changing the composition and a large magnetization variation with respect to temperature near T_c. In literature, Fe-B-Zr based amorphous alloys were found to meet all the desired criteria, exhibiting a soft ferromagnetic behavior with a high saturation magnetization and a Curie temperature tunable by varying the alloy Fe content [17][18]. $\mathrm{Fe}_x\mathrm{B}_{\frac{5}{16}(100-x)}\mathrm{Zr}_{\frac{11}{16}(100-x)}$ $(x = 83, 84, 85, 86)$ compositions were selected, with the intent of producing a series of samples with variable Curie temperatures around 300K.

4.1 Experimental

All the samples were prepared starting by melting the pure elements, nominally weighted to obtain ingots of 5g of total mass, in an Edmund Bühler MAM-1 arc furnace under argon atmosphere of 500mbar. A pre-melt of the required iron was carried out beforehand to separate oxides and impurities,

while boron and zirconium were used without further preparation. Each ingot was flipped and melted three times to improve compositional homogeneity. Between subsequent melts, the ingots' surface was mechanically polished to remove as much oxidation and impurities as possible from the melting process. All the ingots during the final melt were placed in a elongated crucible and were thus given a shape suitable for introduction in the melt spinner quartz tube crucibles.

As a final step, all the samples were melt spun in a Edmund Bühler Melt Spinner SC at a temperature of 1400°C under pure Ar atmosphere. The tanks providing gas to the nozzle for melt ejection were filled with argon at atmospheric pressure, while the main chamber of the melt spinner was filled with argon at a pressure of 700mbar. The rotation speed of the copper wheel was set to 70Hz, corresponding to a surface speed of the wheel of 44m/s.

To characterize the magnetic behavior of the produced samples, SQUID magnetometry experiments were performed, measuring the mass magnetization with respect to temperature and magnetic field intensity. The measurements were carried out in a Quantum Design MPMS-XL SQUID magnetometer and some preliminary measurements were performed using a DC extraction magnetometer, a modified version of the Oxford Instruments Maglab System 8000, equipped with a liquid nitrogen flow cryostat. For each sample, multiple pieces of the melt-spun ribbons were put together to increase the available magnetic signal and reduce the relative error on the weighted sample mass. All the samples were positioned in the magnetometer with the H field in-plane with respect to the ribbon surface.

Finally, several temperature cooling sweeps between 360K and 240K were performed, with increasing values of magnetic field up to 2T, to estimate the magnetic entropy change for all the samples.

For this study, two ring-shaped rotors were prepared from the sample having composition $Fe_xB_{\frac{5}{16}(100-x)}Zr_{\frac{11}{16}(100-x)}$ with x=86 using the as-spun ribbons. Because of the elasticity of the material, it was not possible to grind the ribbons to powders and follow the procedure described in section 2.5 for the

fabrication of composite-based rotors.
For this reason, the thermomagnetic rotors have instead been prepared by directly winding and gluing the as-spun ribbon, of approximately 1 mm width, on a 3D-printed circular plastic support (fig. 4.1).
The fabricated rotors have an diameter of 18mm and a length of approximately 1 mm. The net mass of active magnetic material in the rotors was approximately 0.10±0.01 g and 0.15±0.01 g, respectively.

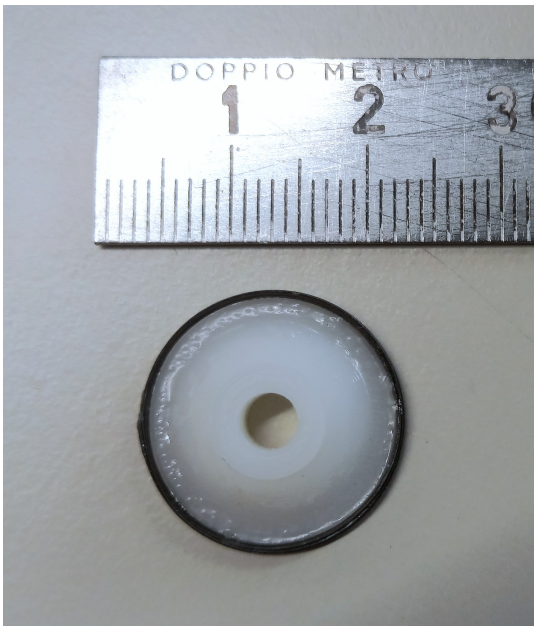

Figure 4.1: Example of rotor made of FeBZr melt-spun alloy.

The in-operando evaluation in the TM motor was performed by recording mechanical power output and rotation speed while varying the resistive load and the temperature of the hot water. The load sweep was conducted in both increasing and decreasing load resistance to verify measurement repeatability. Power versus speed curves were recorded for each rotor by using as cold source the ambient air at a temperature of 297K with natural convection. The rotor was submerged to a depth of 3 mm in the water as in previous experiments conducted on Heusler alloys.

4.2 Results and discussion

4.2.1 X-Ray Diffraction characterization

For each produced composition, a sample was taken from the middle portion of the as-spun ribbon to perform X-ray diffraction experiments in order to identify the material's structure. All the collected diffraction patterns present a single large, broad, diffraction peak at angles 2Θ between 35 and 55 degrees (*amorphous halo*) and a second significantly smaller broad peak between 70 and 85 degrees (fig. 4.2). The absence of narrow diffraction peaks excludes the presence of a long-range structural ordering, confirming the amorphous or nanocrystalline nature of the samples under study.

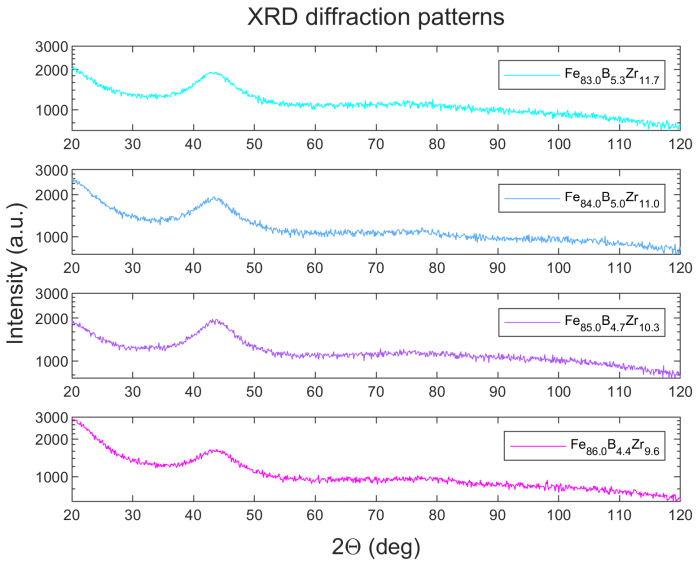

Figure 4.2: X-ray diffraction patterns of the as-spun FeBZr amorphous ribbons.

4.2.2 SEM analisys

To investigate the morphology, thickness and composition of the samples, a SEM microscopy analisys was carried out using a FESEM Zeiss Auriga compact equipped with a Oxford Instruments EDX detector. The SEM morphological analysis didn't show any structures at the micrometer scale. The SE

detector imaging shows areas with different contrast (fig. 4.3), but the EDX composition maps show a uniform distribution of the alloy components also in these areas.
The Fe/Zr ratio from EDX spectra was found to be in good agreement with respect to the nominal compositions within the uncertainty of the instrument. Boron concentration estimations were possible, but the detector in use overestimates boron during quantitative analisys and to get accurate results a reference sample of well known boron content would be needed.
Cross section imaging of the ribbons allowed to measure the thickness of the samples, which resulted to be between 10 and 30 μm (fig. 4.4).

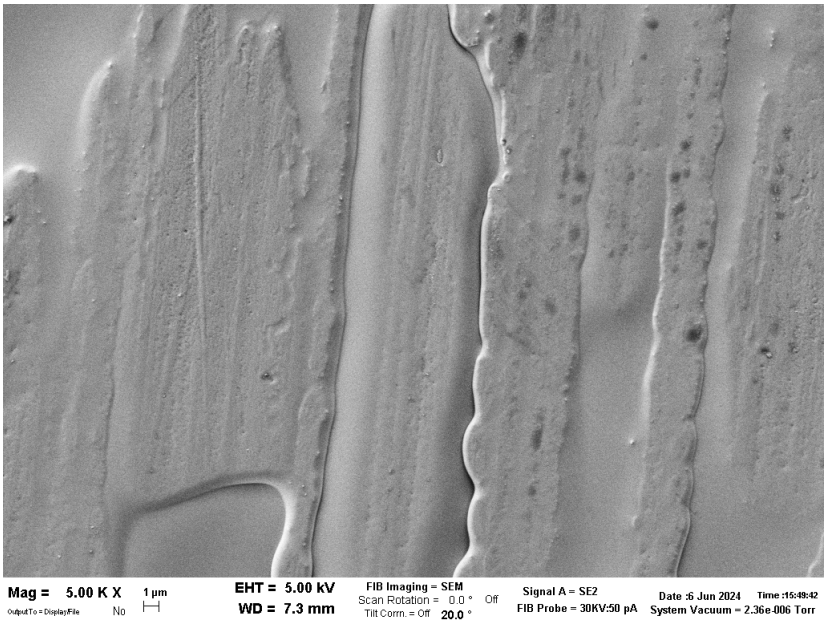

Figure 4.3: SE detector SEM planar image of the sample Fe85.

4.2.3 Magnetometry and magnetic entropy change

The mass magnetization was measured between 380K and 10K for values of $\mu_0 H$ of 1T and 1mT (fig. 4.5 and 4.6), in both cooling and heating temperature ramp modes.

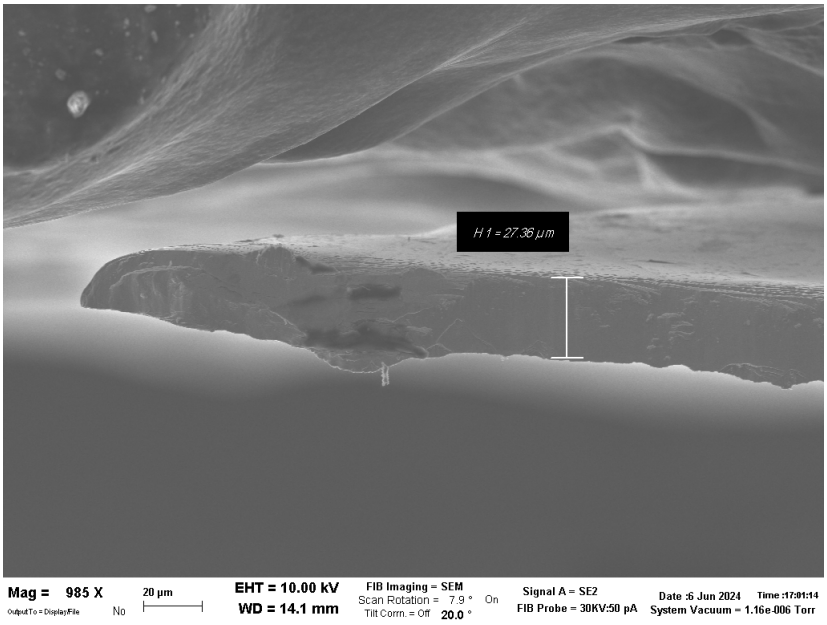

Figure 4.4: Cross-section SEM image of the sample Fe85 used to estimate ribbon thickness.

All the samples exhibit a relatively sharp second order Curie transition, without signs of the presence of secondary magnetic phases or other magnetic or magnetostructural transitions.
A thermal hysteresis of approximately 1K was observed between cooling and heating M(T) measurements and should be attributed to the thermal inertia of the sample holder.
The magnetization values collected at 10K with an applied field of $\mu_0 H$=1T were taken as an estimate of the saturation magnetization. All the saturation magnetization M_s values obtained are relatively high, above 120emu/g, with a mild correlation with respect to the iron content of the alloys.
The derivative of the mass magnetization with respect to temperature was computed for each sample starting from the M(T) measurement data collected at $\mu_0 H$=1mT (fig. 4.7) and the temperature value of its minimum was taken as an estimate of the Curie temperature T_c. The produced sample series shows the desired tuning of the T_c, with a Curie temperature that increases while decreasing the alloy Fe content at a rate of approximately

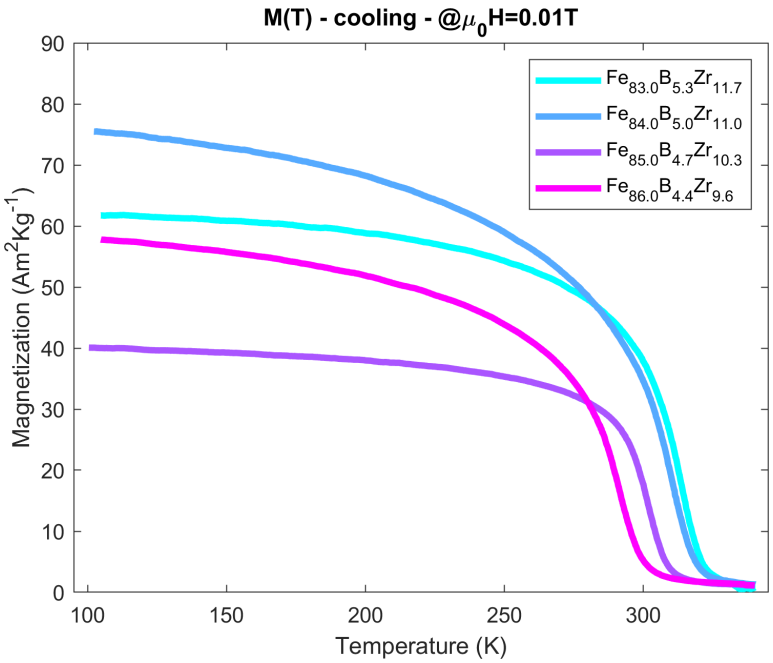

Figure 4.5: Magnetization measurements of the as-spun FeBZr amorphous alloys vs temperature with μ_0H=0.01T.

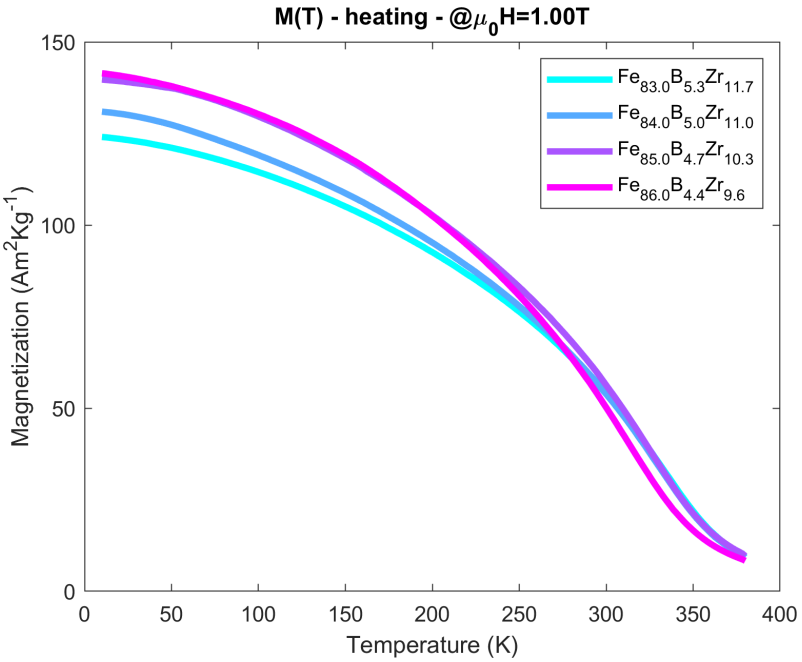

Figure 4.6: Magnetization measurements of the as-spun FeBZr amorphous alloys vs temperature with μ_0H=1T.

8K/% (fig. 4.8).

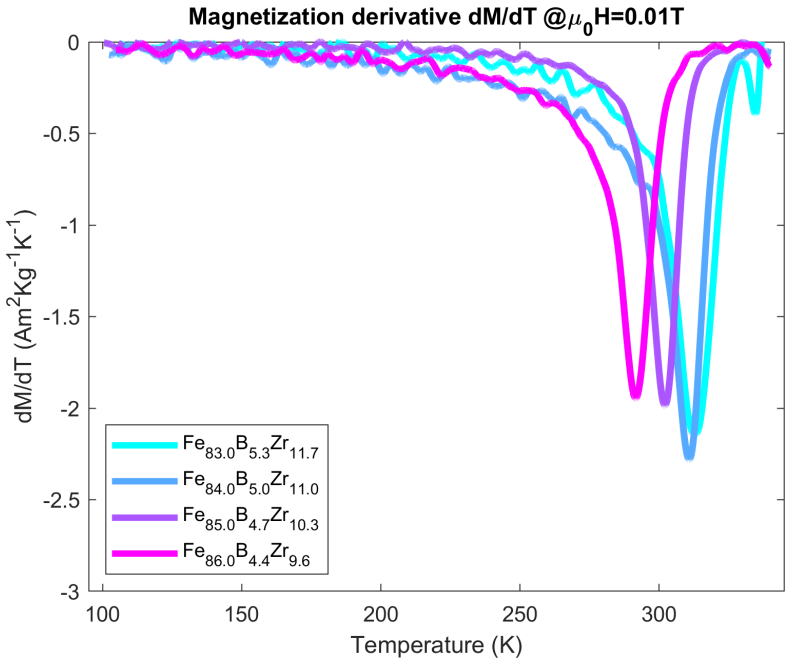

Figure 4.7: Computed magnetization derivative with respect to T of the studied FeBZr amorphous alloys.

At 340K and 100K magnetic 5-segments hysteresis loops were measured for each sample to further investigate the nature of the magnetism above and below the Curie temperature T_c, starting from H=0 and up to $\mu_0 H$=1.2T in absolute value (fig. 4.9). All the samples show below T_c an excellent soft-magnetic behaviour, with a coercivity below $5 \cdot 10^{-5}$T ($40 A/m^2$) (fig. 4.10 and 4.11). Above T_c, all the samples exhibit paramagnetic behaviour.
Regarding the magnetic entropy change associated to a magnetic field variation from 0 to 2T, all the samples showed a broad peak in correspondence of the T_c, with a maximum value of ΔS of approximately $-1.6 JKg^{-1}K^{-1}$ almost independent from the composition (fig. 4.12). This kind of measurement is meaningful in the context of thermomagnetic energy harvesting since the integral of the ΔS curve between two different temperatures represents the magnetic work produced by a TM cycle operating between those two temperatures.

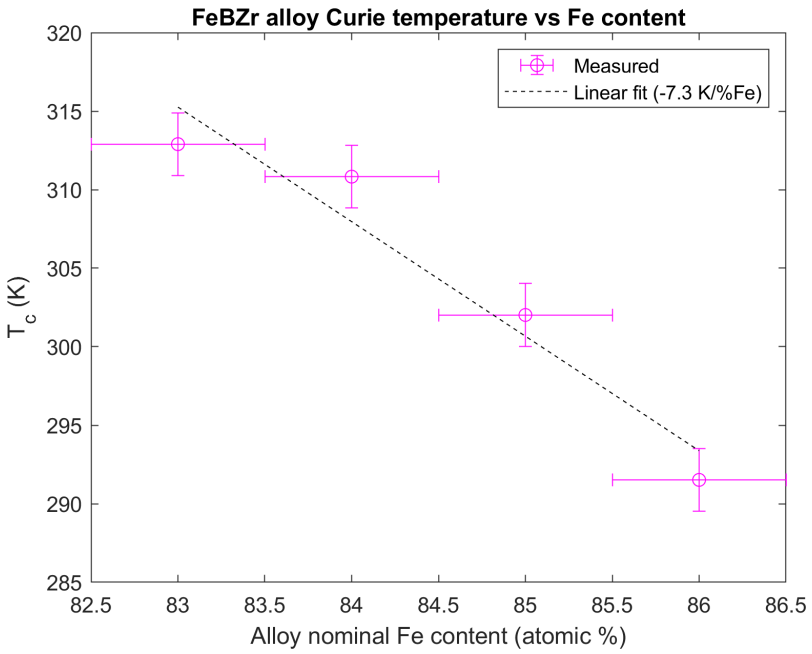

Figure 4.8: Estimated Curie transition temperature of the studied FeBZr amorphous alloys vs iron content percentage.

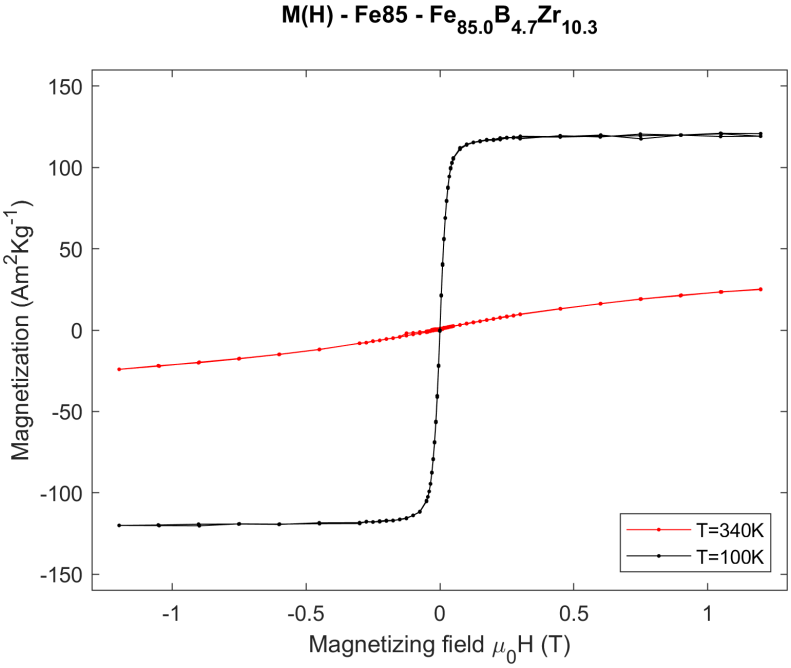

Figure 4.9: Magnetization vs magnetic field H of the studied FeBZr amorphous alloy $\mathrm{Fe}_x\mathrm{B}_{\frac{5}{16}(100-x)}\mathrm{Zr}_{\frac{11}{16}(100-x)}$ with x=85.

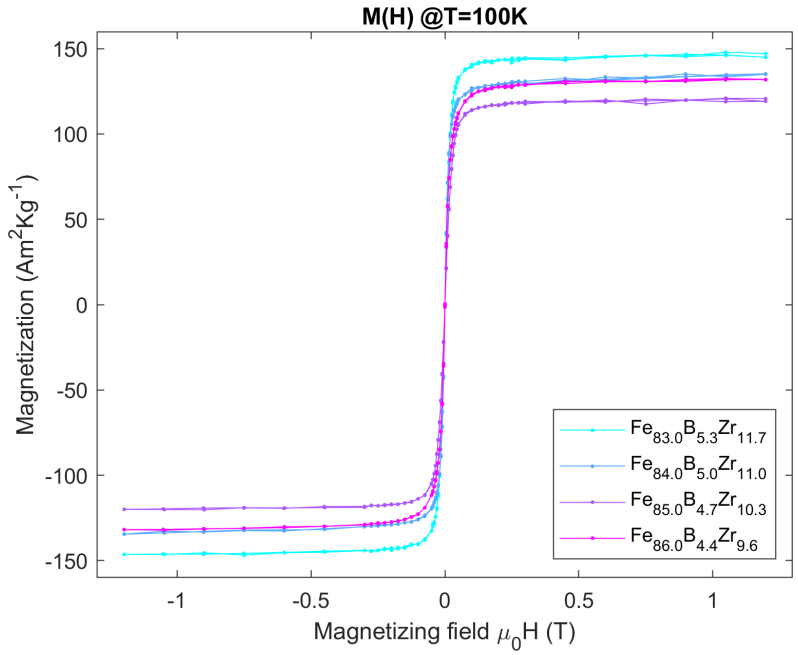

Figure 4.10: Magnetization vs magnetic field H of the studied FeBZr amorphous alloys.

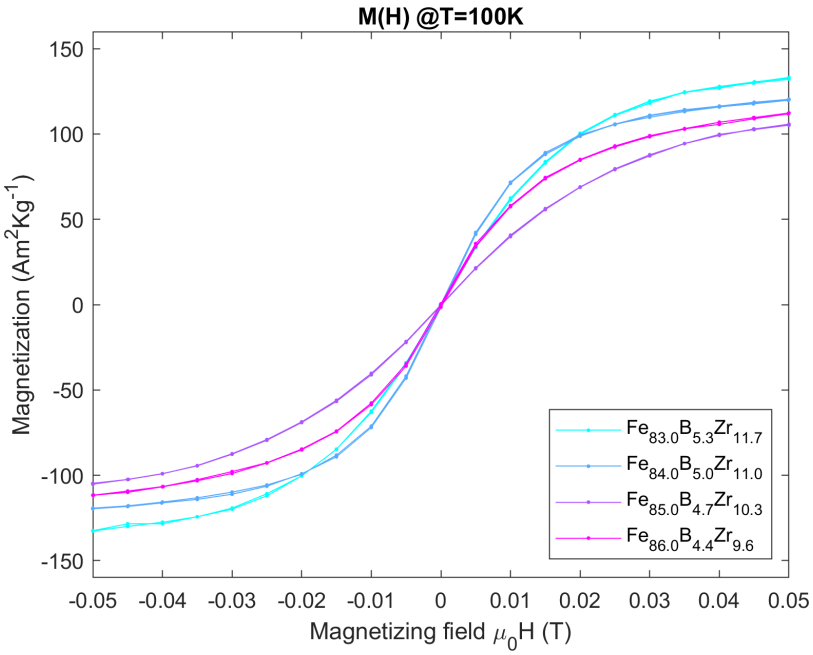

Figure 4.11: Magnetization vs magnetic field H of the studied FeBZr amorphous alloys, detail.

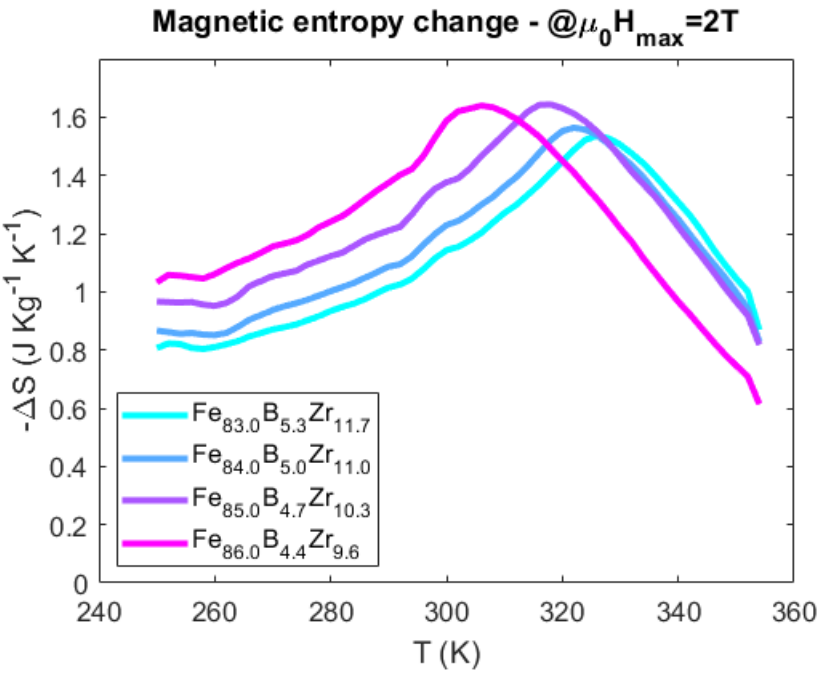

Figure 4.12: Magnetic entropy change ΔS of the studied FeBZr amorphous alloys corresponding to a magnetic field change from 0 to 2T.

4.2.4 In operando evaluation for TMG

Figure 4.13 shows the mechanical power output as a function of the angular speed for the tested rotors at three different values of T1, while maintaining the cold side room temperature constant at 297 K. Generally, the power output increases as the temperature of the warm heat source increases, but rapidly saturates when T1 exceeds 318K; this result resembles the experiments carried out on NiMnCuGa and in a similar way should be attributed to the low T_c of the chosen composition for the active material.
Also for these samples, power output varies with the rotation speed, showing an optimum speed of $\omega = 1.6 \text{rad} s^{-1}$ at which the maximum mechanical power output of $4.6 \cdot 10^{-5} W$ is produced, corresponding to 0.18±0.02 W/Kg of active material (fig. 4.13).

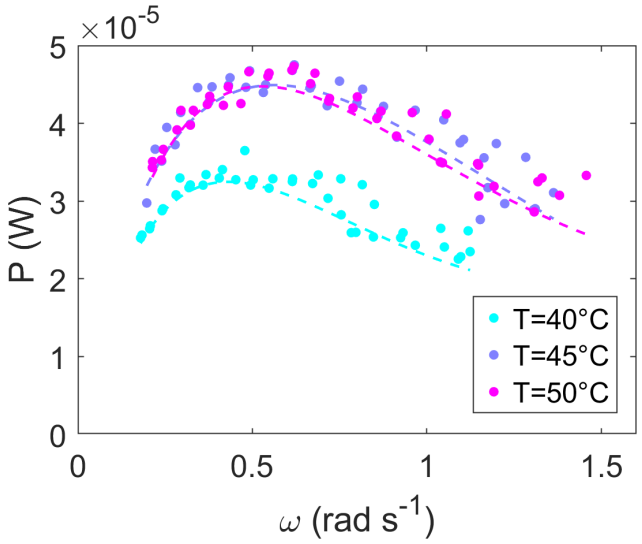

Figure 4.13: Mechanical power output of the TM motor prototype as a function of the shaft speed obtained by varying the temperature of the warm source (T1) and the external resistive load exploiting two rotors of composition $\text{Fe}_x\text{B}_{\frac{5}{16}(100-x)}\text{Zr}_{\frac{11}{16}(100-x)}$ with x=86.

Chapter 5

MnFePSi alloys

In collaboration with Delft University of Technology (NL)

A series of samples of the $Mn_xFe_{2-x}P_{1-y}Si_y$ family of compounds was prepared by high energy ball milling to test the capabilities of these materials for thermomagnetic energy harvesting applications.
This family of compounds has been widely studied for magnetic refrigeration applications, showing a sharp ferromagnetic to paramagnetic transition at the critical temperature. Changes in the Mn to Fe and P to Si ratios allow the tuning of the Tc over a wide temperature range; for certain compositions, however, a huge thermal hysteresis is observed, and also considerable quantities of secondary crystalline phases can be present[21].
The compositional formula $Mn_xFe_{2-x}P_{0.4}Si_{0.6}$ (x=1.32,1.27,1.23,1.18) was chosen to obtain a series of four samples with increasing Tc in the range between 300K and 340K; the Si to P ratio was selected to achieve the lowest possible thermal hysteresis for the required Tc range, but as a tradeoff about 15% weight fraction of secondary phases is expected[21].

5.1 Experimental

The samples have been prepared by high energy ball milling of the raw materials in powder form, namely Mn (99.7%), Fe (99.8%), FeP (Fe 70 wt.%,

P 25.7 wt.%), Si (99.6%), using 80ml steel jars (fig. 5.1) under argon atmosphere. A balls-to-sample mass ratio of 4:1 was used, introducing in the jars one 4g steel milling ball for each gram of final product to be prepared. The milling process was carried out for a total time of 10 hours at a speed of 380rpm using a Fritch Pulverisette 5 mill.

Figure 5.1: Steel jar for high energy ball milling containing precursor powders and milling balls before starting the milling process.

The powders collected after the milling process were compressed into pellets, sealed in quartz ampoules under argon atmosphere and underwent an annealing process for 24 hours at 1100°C. After the annealing, all the samples were quenched into water.
The samples obtained from the annealing were then hand-ground to powders using a steel mortar. Liquid nitrogen was used to make the samples more brittle and help the grinding process.
All the samples have been characterized by x-ray powder diffraction experiments using a PANalytical X'Pert Pro diffractometer and the diffraction patterns were analyzed by Rietveld refinement using the FullProf suite[22][23] to confirm the desired crystal structure has been obtained and assess the fracion of secondary phases.
The samples' magnetic properties have then been characterized using a Quan-

tum Design MPMS-XL Squid magnetometer. Temperature swept magnetization measurements in a field of 10mT were used to estimate the critical temperature T_c and the thermal hysteresis of the produced materials. The samples needed to be prepared by placing a small amount of powders on the adhesive side of a piece of kapton tape to avoid rearrangement and reorientation of the powder grains.

Multiple M(T) measurements were performed at increasing values of applied magnetic field up to 2T in order to estimate the magnetic entropy change ΔS for a magnetic field change from 0 to 2T.

For this study, we prepared ring-shaped rotors for in-operando evaluation for each of the four investigated compositions. The rotors have an external diameter of 20 mm, an internal diameter of 18mm and a length of 1 mm. Utilizing a composite with 85±2 wt% magnetic powder, the net mass of active magnetic material in the rotors is approximately 0.21±0.01g.

The evaluation of the four material compositions in the TM motor was performed recording mechanical power output, electric power output and rotation speed while varying the resistive load and the temperature of the hot water. As in previous experiments of the same type, the load sweep was conducted in both increasing and decreasing load resistance to verify measurement repeatability. Power versus speed curves were recorded for each rotor by using as cold source the ambient air at a temperature of 298K under natural convection. The rotor was submerged to a depth of 3 mm in the water to obtain the same thermal gradient as in the previous experiments.

The overall efficiency of the device in the conversion from thermal to electric power was estimated by taking the ratio between electric power output and the electric power provided to the heater resistor that simulates the waste heat source in the prototype.

5.2 Results and discussion

5.2.1 X-Ray Diffraction characterization

The Rietveld analysis of the XRD patterns (fig. 5.2) allowed to estimate a main hexagonal Fe_2P-type P-62m phase content of approximately 82 wt.%, in good agreement with data reported in literature[21]. Similarly to other reported results[21], the recorded diffraction patterns contain extra peaks due to the presence of a cubic Fe_3Si-type structure (Fm-3m) and an hexagonal Mn_5Si_3-type structure (P63/mcm) with a weight fraction of approximately 12% and 6% respectively.

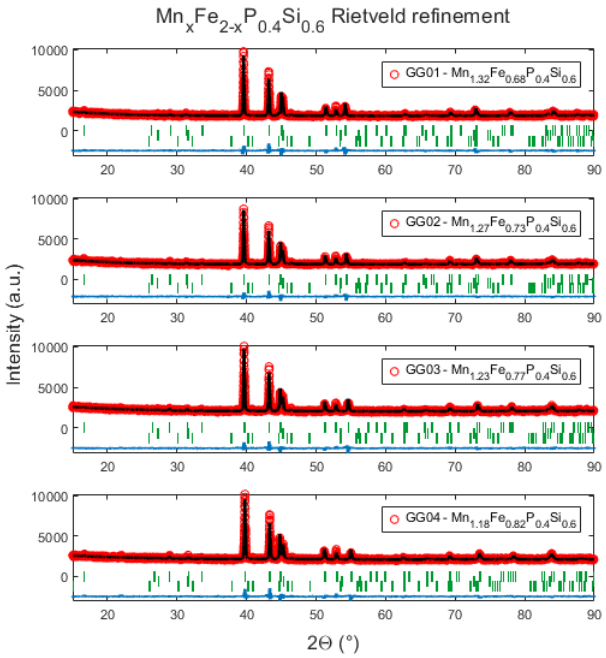

Figure 5.2: X-ray powder diffraction patterns of the samples with composition $Mn_xFe_{2-x}P_{0.4}Si_{0.6}$ (x=1.32,1.27,1.23,1.18).

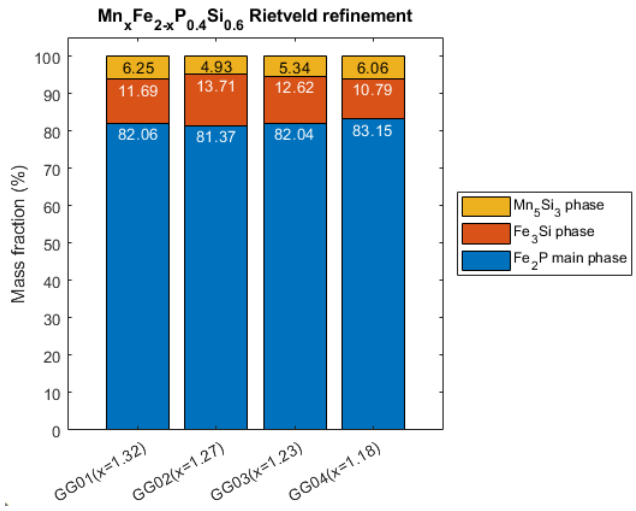

Figure 5.3: Phase composition estimate obtained by Rietveld refinement of the XRD patterns for samples $Mn_xFe_{2-x}P_{0.4}Si_{0.6}$ (x=1.32,1.27,1.23,1.18).

5.2.2 Magnetometry and magnetic entropy change

Measurements of M(T) in 1T magnetic field (fig. 5.4) confirm a high low-temperature saturation magnetization above $100 Am^2Kg^{-1}$ for the entire sample series and also a considerable dM/dT above $2 Am^2Kg^{-1}T^{-1}$ at the critical temperature. Low-field temperature-swept magnetization measurements in a 10mT magnetic field (fig. 5.5) show a sharp magnetic phase transition above room temperature and confirm that the tuning of the T_c by means of changing the Mn and Fe content of the alloy was successfully achieved; in all the samples, the observed thermal hysteresis resulted to be less than 2K. At temperatures lower than 150K, traces of other magnetic phase transitions are observable and can be attributed to the presence of secondary phases.
Regarding the magnetic entropy change associated to a magnetic field variation from 0 to 2T, all the samples showed a narrow peak in correspondence of the T_c, with a maximum value of ΔS ranging from -4 to $-5.5 JKg^{-1}K^{-1}$ (fig. 5.6).

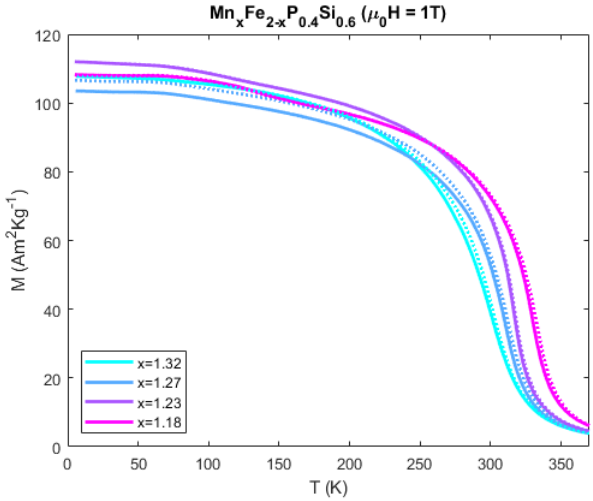

Figure 5.4: Magnetization in 1T applied magnetic field as a function of temperature for the alloys with composition $Mn_xFe_{2-x}P_{0.4}Si_{0.6}$ (x=1.32,1.27,1.23,1.18).

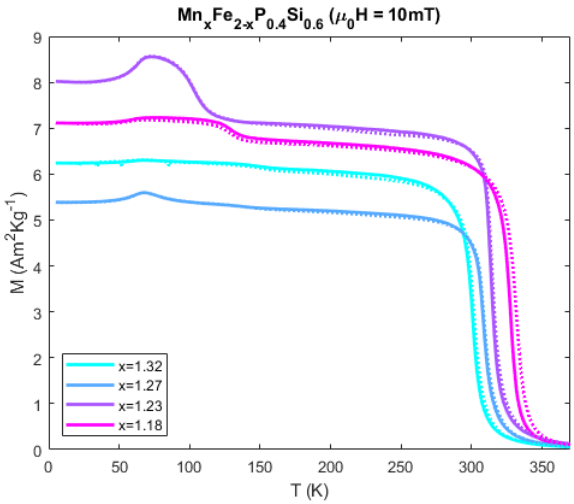

Figure 5.5: Low-field magnetization in 10mT applied magnetic field as a function of temperature for the alloys with composition $Mn_xFe_{2-x}P_{0.4}Si_{0.6}$ (x=1.32,1.27,1.23,1.18).

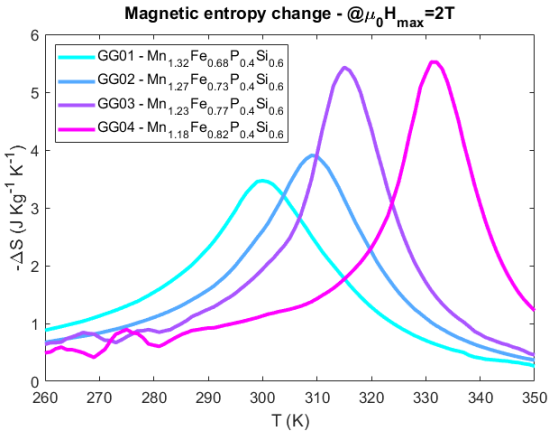

Figure 5.6: Magnetic entropy change ΔS for the alloys with composition $Mn_xFe_{2-x}P_{0.4}Si_{0.6}$ (x=1.32,1.27,1.23,1.18) corresponding to a magnetic field change from 0 to 2T.

5.2.3 In operando evaluation for TMG

Figure 5.7 compares, as an example, mechanical and electric power output with respect to rotation speed for a rotor of composition $Mn_{1.23}Fe_{0.77}P_{0.4}Si_{0.6}$ at a temperature of the warm source (T1) of 323K, while maintaining the cold side room temperature constant at 298 K under natural convection. The mechanical to electric power conversion efficiency varies with angular speed, but it is worth to observe that efficiency up to 70% can be achieved with the designed prototype. As with other tested thermomagnetic materials, mechanical power output initially increases with ω, then reaches a maximum and finally decreases at higher rotation speed, showing that an optimal working regime exists for the device during operation. Figure 5.8 shows that generally power output also initially increases with increasing warm source temperature and then saturates.

Figure 5.9 compares the maximum obtained mechanical power output as a function of T1 for the four MnFePSi compositions under investigation. For all the samples, a sudden rise in power output is observed as the warm source temperature T1 of the device is increased above the critical temperature T_c of the material contained in the rotor; when further increasing the warm side

temperature of the thermomagnetic motor, power output rapidly saturates or even drops.

This result highlights that material performance heavily depends on the critical temperature of the material and the real temperatures of the thermomagnetic cycle, confirming the need to specifically tune the material T_c considering the working temperatures of the device for each different application case.

For the MnFePSi material family, with the investigated compositions, the best-performing configuration was found to be using a rotor containing active material of composition $Mn_{1.18}Fe_{0.82}P_{0.4}Si_{0.6}$, with a T_c of 333K, setting the warm side temperature of the device to 338K and with a room temperature of 300K on the cold side of the machine. Under these conditions, the maximum measured power output, found at a speed of $\omega = 3 \text{rad} s^{-1}$, amounts to $2 \cdot 10^{-4} W$, corresponding to 1.0±0.1 W/Kg of employed active material. The estimated overall thermal to electric energy conversion efficiency of the device in the same conditions was of $3 \cdot 10^{-5}$, which corresponds to 0.03% of the Carnot efficiency for the same working temperatures.

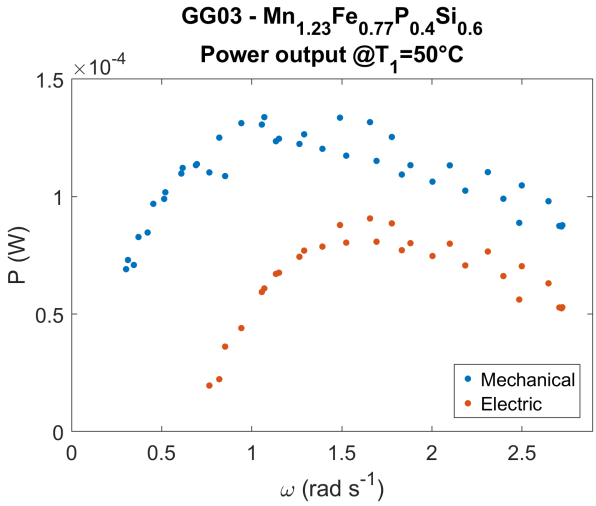

Figure 5.7: Comparison of mechanical and electric power output of the TM motor prototype as a function of the shaft speed obtained by varying the external resistive load exploiting rings of composition $Mn_{1.23}Fe_{0.77}P_{0.4}Si_{0.6}$ at a temperature of the warm source (T1) of 323K.

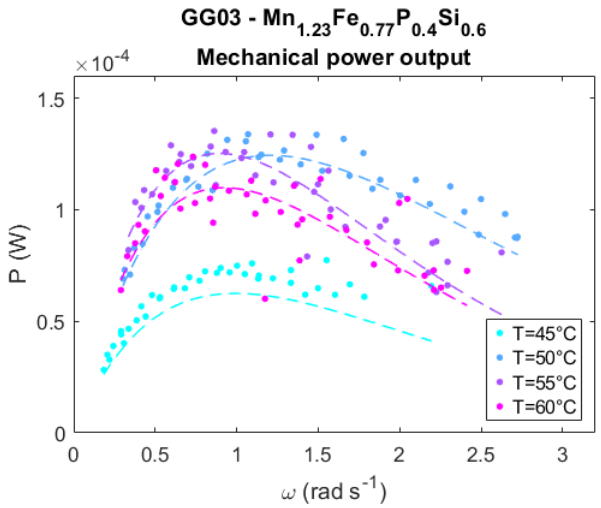

Figure 5.8: Mechanical power output of the TM motor prototype as a function of the shaft speed obtained by varying the temperature of the warm source (T1) and the external resistive load exploiting rings of composition $Mn_{1.23}Fe_{0.77}P_{0.4}Si_{0.6}$.

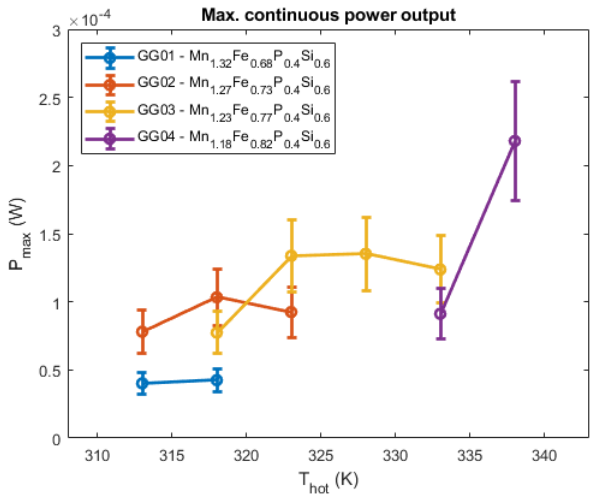

Figure 5.9: Maximum mechanical power output as a function of temperature T1 of the warm reservoir for a rings of 1 mm thickness containing $Mn_xFe_{2-x}P_{0.4}Si_{0.6}$ (x=1.32,1.27,1.23,1.18). Solid lines serve as guide to the eyes.

Chapter 6

$Mn_5(Si,P)B_2$ alloys

In collaboration with Delft University of Technology (NL)

A series of four samples of the $Mn_5(Si_{1-x}, P_x)B_2$ family of compounds was prepared by high energy ball milling and studied as a low cost candidate material for low grade waste heat thermomagnetic energy harvesting applications. This family of compounds typically shows a second order ferromagnetic to paramagnetic transition at a critical temperature T_c which can be easily tuned in the range between 300K and 400K by modifying the P and Si content of the alloy, which represents an optimal characteristic for the use in waste heat harvesting applications[24].
The compositional formula $Mn_5(Si_{1-x}, P_x)B_2$ (x=0.99,0.93,0.87,0.83) was chosen to obtain a series of four samples with increasing Tc in the range between 303K and 318K.

6.1 Experimental

The samples have been prepared by high energy ball milling of the raw materials, namely Mn (99.7%), MnP (Mn 63 wt.%, P 33.1 wt.%), Si (99.6%), B (99.8%) using 80ml steel jars (fig. 6.1) under argon atmosphere.
Since all the raw materials consisted in powders, except for boron which was available in form of solid pieces, a quantity close to the required amount of

boron was first weighed; then the required quantities for the remaining raw materials were re-calculated and weighed accordingly.
A balls-to-sample mass ratio of 4:1 was used, introducing in the jars one 4g steel milling ball for each gram of final product to be prepared. The milling process was carried out for a total time of 10 hours at a speed of 350rpm using a Fritch Pulverisette 5 mill.

Figure 6.1: Steel jar for high energy ball milling containing precursor powders and milling balls before starting the milling process.

For the two samples corresponding to x=0.93 and x=0.87 the milling process did not completely grind the boron pieces, resulting in an incomplete incorporation of the boron mass in the alloy; those compositions were then re-prepared by pre-grinding the boron pieces by hand using an agate mortar and the speed for the milling process was increased from 350 to 380rpm while keeping the same total milling time.
The powders collected after the milling process were compressed into pellets, sealed in quartz ampoules under argon atmosphere and underwent an annealing process for 24 hours at 1130°C. After the annealing, all the samples were quenched into water.
The samples obtained from the annealing were then hand-ground to powders using a steel mortar. Liquid nitrogen was again used to make the samples more brittle and help the grinding process.

All the samples have been characterized by X-ray powder diffraction experiments using a PANalytical X'Pert Pro diffractometer and the diffraction patterns were analyzed by Rietveld refinement using the FullProf suite[22][23] to confirm the desired crystal structure has been obtained and assess the fracion of secondary phases.
The samples' magnetic properties have then been characterized using a Quantum Design MPMS-XL Squid magnetometer. Temperature swept magnetization measurements in a field of 10mT were used to estimate the critical temperature Tc and the thermal hysteresis of the produced materials. All samples were prepared for SQUID magnetometry measurements by placing a small amount of powders on the adhesive side of a piece of kapton tape to avoid rearrangement and reorientation of the powder grains.
Multiple M(T) measurements were performed at increasing values of applied magnetic field up to 2T in order to estimate the magnetic entropy change ΔS for a magnetic field change from 0 to 2T.

6.2 Results and discussion

6.2.1 X-Ray Diffraction characterization

The Rietveld analysis of the XRD patterns (fig. 6.2) allowed to estimate a main tetragonal Cr_5B_3-type I4/mcm phase content of approximately 92 wt.% for the purest sample, in good agreement with data reported in literature[24]. Similarly to previously reported results[24], the recorded diffraction patterns contain additional peaks due to the presence of a hexagonal Mn_2P-type secondary phase with P-62m space group. The remaining diffraction peaks are explained considering a third orthorombic Mn_5B-type structure (Pnma) secondary phase.
For the samples that were reprepared at higher milling speed, a higher main phase fraction was observed, along with a significantly smaller fraction of the MnB secondary phase, suggesting that increasing milling speed and reducing the grain size of the starting raw materials can be beneficial for the phase

purity of the product.

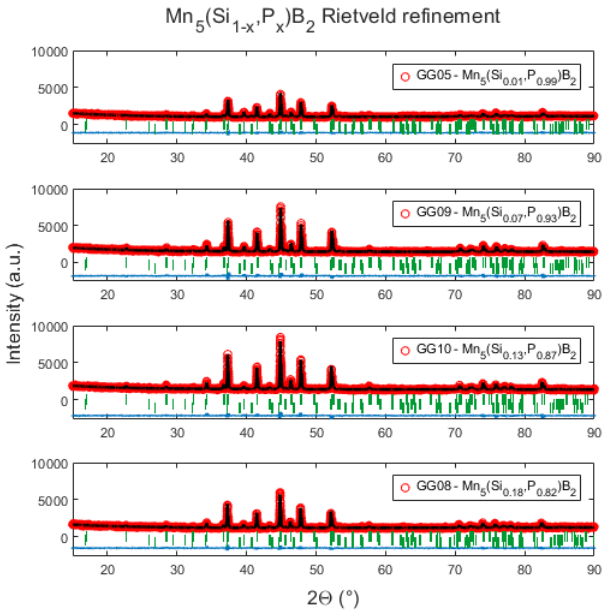

Figure 6.2: X-ray powder diffraction patterns of the samples with composition $Mn_5(Si_{1-x}, P_x)B_2$ (x=0.99,0.93,0.87,0.83).

6.2.2 Magnetometry and magnetic entropy change

Measurements of M(T) in 1T magnetic field (fig. 6.4) confirm a high low-temperature saturation magnetization above $85 Am^2 Kg^{-1}$ that increases up to $100 Am^2 Kg^{-1}$ while decreasing the atomic P content of the alloy from 0.99 to 0.83. Low-field temperature-swept magnetization measurements in a 10mT magnetic field (fig. 6.5) show a single magnetic phase transition above room temperature with no thermal hysteresis and confirm that the tuning of the T_c by means of changing the Si and P content of the alloy was successfully achieved.

Regarding the magnetic entropy change associated to a magnetic field variation from 0 to 2T, all the samples showed in correspondence of the T_c a broad peak due to the second order nature of the magnetic phase transition,

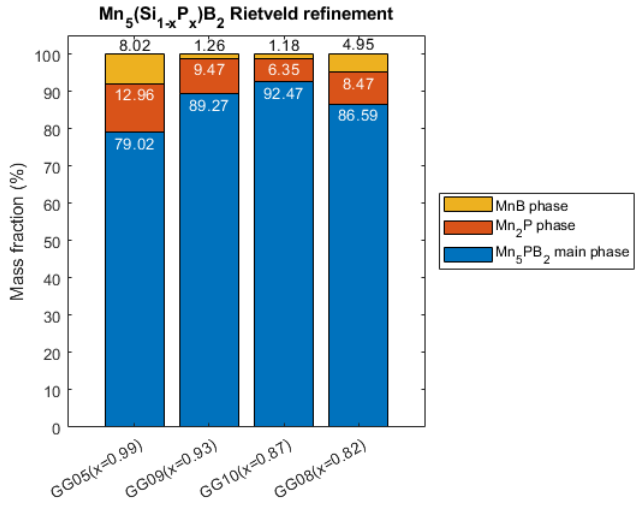

Figure 6.3: Phase composition estimate obtained by Rietveld refinement of the XRD patterns for samples $Mn_5(Si_{1-x}, P_x)B_2$ (x=0.99,0.93,0.87,0.83).

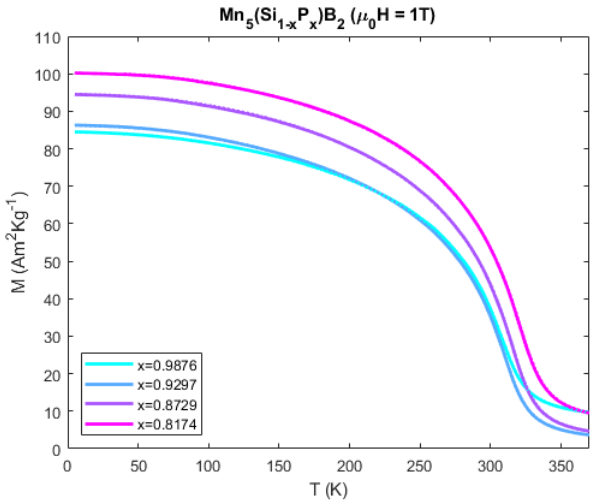

Figure 6.4: Magnetization in 1T applied magnetic field as a function of temperature for samples $Mn_5(Si_{1-x}, P_x)B_2$ (x=0.99,0.93,0.87,0.83).

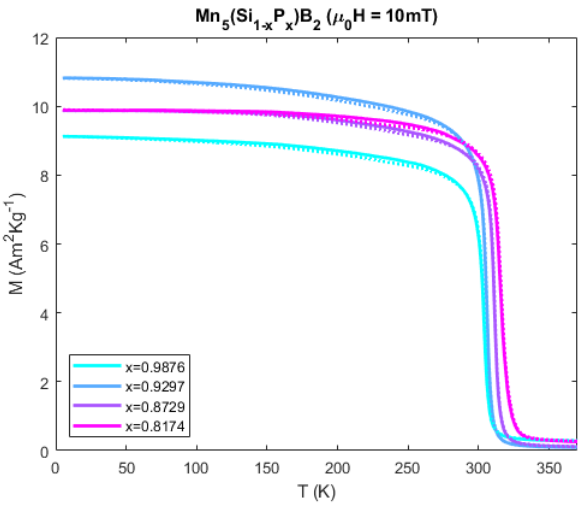

Figure 6.5: Low-field magnetization in 10mT applied magnetic field as a function of temperature for samples $Mn_5(Si_{1-x}, P_x)B_2$ (x=0.99,0.93,0.87,0.83).

with a maximum value of ΔS ranging from -2.3 to $-3 JKg^{-1}K^{-1}$ almost independently from the composition (fig. 6.6). This characteristic makes this compound family a promising candidate to be tested for use in thermomagnetic harvesting applications in which the device needs to be able to operate in a wide warm side temperatures range.

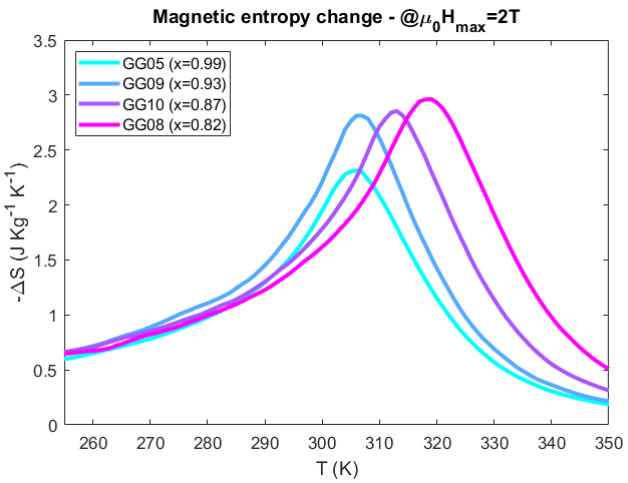

Figure 6.6: Magnetic entropy change ΔS for samples $Mn_5(Si_{1-x}, P_x)B_2$ (x=0.99,0.93,0.87,0.83) corresponding to a magnetic field change from 0 to 2T.

Chapter 7

Conclusions and perspective

This work investigated the potential of four families of materials, Ni,Mn-based Heusler alloys, FeBZr amorphous alloys, $Mn_xFe_{2-x}P_{0.4}Si_{0.6}$ crystalline alloys and $Mn_5(Si_{1-x}, P_x)B_2$ alloys for thermomagnetic harvesting of low-grade waste heat in the temperature range of 300 – 340 K.
Their performance was directly measured in a novel thermomagnetic tester designed for in-operando evaluation of TM materials under various conditions. This small-scale prototype of thermomagnetic motor allows for testing small sample masses (less than 0.3 g), typical of laboratory-scale material science experiments, and serves as a crucial bridge between fundamental material research and prototypes development. The tester can measure the mechanical output power of the TM motor as a function of the thermal sources temperatures and of the rotational speed, which is varied by applying an external electronic load, allowing to assess the behavior of the device in different dynamic conditions. The variation of thermal sources temperature and rotation speed, which control heat exchanges, allows to experimentally realize TM cycles with different thermal spans and evaluate the optimal thermomagnetic performance of each material.
This is important to test materials characterized by different magnetization gradients with temperature and materials undergoing a first-order magnetic transition characterized by hysteresis and irreversibility effects. In general, all

promising thermomagnetic materials that can be reduced to a coarse powder with maximum grain size smaller than 200 µm can be implemented and tested in the prototype. This was made possible by a straightforward and repeatable method specifically developed for producing small and dimensionally precise ring-shaped rotors, which relies on epoxy-based composites and 3D-printed soluble molds. The use of additive manufacturing for producing the molds possibly allows to obtain complex rotor shapes and facilitates the evaluation on different rotor designs.

The capability of the TM tester to continuously monitor the rotational speed and torque of the rotor enables the indirect assessment of the homogeneity of the prepared rotors and the verification of potential long-term deterioration effects. Moreover, the precise measurement of the mechanical and of the electric power output achievable by connecting the TM motor to an electric generator underscored the potential of the realized TM energy converter design.

To further enhance the performance of the TM motor it is necessary to independently test and optimize its various components (geometry and material of the active rotor, magnetic field source, heat exchange medium and spatial distribution of the thermal gradient, mechanical-to-electric energy converter). This objective can be accomplished thanks to the flexibility and modularity of the presented prototype, which can also serve as a test-bench for TMG designs.

In this work, a preliminary study on the geometries of the active elements was performed when testing Heusler alloys as active materials. Three configurations of the active element were examined, revealing that, with characteristics length scales of 1 mm, the bottleneck restricting the output mechanical power of the thermomagnetic motor is the heat exchange at the interface with the heat transfer fluids and inside the composite thermomagnetic material. This result highlights the need for further effort to design active elements with an increased surface to volume ratio and improve heat conduction in TM epoxy-based composites.

A critical aspect to address in the future will be the accurate determination of the temperatures reached by the material during the cycle. This measurement is crucial for completing the in-operando characterization process for thermomagnetic materials, allowing to obtain the effective temperatures reached by the TM cycle during operation. Achieving this, along with multiphysics finite element simulations, will allow to optimize the geometry and thermal properties of the thermomagnetic generator, enhancing the thermomagnetic performance of the material and of the harvester device itself. Additionally, it would enable the accurate calculation of the heat absorbed by the magnetic material within the thermomagnetic cycle and the efficiency of the thermomagnetic energy conversion process. Also, each element of the prototype (i.e.: the magnets assembly, the relative position of water level and field gradient, the electric generator) needs to be independently characterized, optimized and tested in order to improve power generation performance and efficiency of the device and increase the fraction of magnetic energy that is converted in mechanical and electrical energy.

From the material science point of view, it is not possible to pinpoint a single best-performing TM material for low-grade waste heat harvesting. All the experiments presented in this work agree in pointing out that to improve the performance of this kind of devices the active material must be chosen, and its properties optimized, starting from the critical temperature T_c, according to the real working conditions for a specific application.

Experiments performed on the selected Heusler alloys demonstrated the possibility to use these materials in TMG devices and first revealed the importance of the material critical temperature T_c in relation to the device working temperatures; they also served as a test bench for the TM rotor fabrication process using epoxy-based composites, which is crucial to overcome the limitations caused by the poor mechanical properties of many TM materials.

The measurements carried out on FeBZr metallic glasses obtained by melt spinning demonstrate for the first time that these materials constitute good candidates for thermomagnetic energy conversion applications; their excel-

lent elasticity allows to directly fabricate TM rotors from the as-spun ribbons, thus greatly reducing the thermal properties degradation that is otherwise introduced by the use of an epoxy matrix when working with composites. For the studied class of iron-based metallic glasses, containing a considerable amount of boron in the composition, additional investigation with techniques complementary to SEM EDX is necessary to confirm the effective alloys compositions.

The results collected by in-operando evaluation of $Mn_xFe_{2-x}P_{0.4}Si_{0.6}$ alloys obtained by high energy ball milling prove that this class of materials constitute an excellent low-cost, critical elements-free candidate for thermomagnetic energy harvesting applications. Further work in this direction will include efforts to optimize the material composition and the annealing conditions to minimize the presence of secondary crystalline phases in the alloy. When operated with MnFePSi alloys, the electric power output of the prototype significantly exceeded that achieved in other Curie wheels and static TMGs, highlighting the potential of the developed device.

Finally, a preliminary evaluation of $Mn_5(Si_{1-x}, P_x)B_2$ alloys synthesized by high energy ball milling shows that these compounds also represent a promising candidate for low grade waste heat harvesting, showing a critical temperature T_c that can be easily tuned exactly in the temperature range of interest. Also, the wide second order transition constitutes a favorable characteristic to design devices able to operate in a wide range of warm and cold-side temperatures. Future work on these compounds will involve a complete in-operando characterization of the produced samples in the developed TMG device already presented in this work.

Bibliography

[1] Daniel Dzekan, Anja Waske, Kornelius Nielsch, and Sebastian Fähler. Efficient and affordable thermomagnetic materials for harvesting low grade waste heat. *APL Materials*, 9(1):011105, 2021.

[2] Chiara Coppi, Francesco Cugini, Giacomo Magnani, Chiara Milanese, Lucia Nasi, Laura Lazzarini, Daniele Pontiroli, Mauro Riccò, and Massimo Solzi. Graphene-based magnetocaloric composites for energy conversion. *Advanced Engineering Materials*, 25(1):2200811, 2023.

[3] F. Cugini, L. Gallo, G. Garulli, D. Olivieri, G. Trevisi, S. Fabbrici, F. Albertini, and M. Solzi. In-operando test of tunable heusler alloys for thermomagnetic harvesting of low-grade waste heat. *Acta Materialia*, 288:120847, 2025.

[4] Daniel Champier. Thermoelectric generators: A review of applications. *Energy Conversion and Management*, 140:167–181, 2017.

[5] Miguel Araiz, Álvaro Casi, Leyre Catalán, Álvaro Martínez, and David Astrain. Prospects of waste-heat recovery from a real industry using thermoelectric generators: Economic and power output analysis. *Energy Conversion and Management*, 205:112376, 2020.

[6] Ravi Anant Kishore and Shashank Priya. A review on design and performance of thermomagnetic devices. *Renewable and Sustainable Energy Reviews*, 81:33–44, 2018.

[7] Andrej Kitanovski. Energy applications of magnetocaloric materials. *Advanced Energy Materials*, 10(10), 2020. Cited by: 455; All Open Access, Hybrid Gold Open Access.

[8] Ravi Anant Kishore, Brenton Davis, Jake Greathouse, Austin Hannon, David Emery Kennedy, Alec Millar, Daniel Mittel, Amin Nozariasbmarz, Min Gyu Kang, Han Byul Kang, Mohan Sanghadasa, and Shashank Priya. Energy scavenging from ultra-low temperature gradients. *Energy Environ. Sci.*, 12:1008–1018, 2019.

[9] Yutaka Takahashi, Tomohiro Matsuzawa, and Masahiro Nishikawa. Fundamental performance of the disc-type thermomagnetic engine. *Electrical Engineering in Japan*, 148(4):26–33, 2004.

[10] Marcel Gueltig, Frank Wendler, Hinnerk Ossmer, Makoto Ohtsuka, Hiroyuki Miki, Toshiyuki Takagi, and Manfred Kohl. High-performance thermomagnetic generators based on heusler alloy films. *Advanced Energy Materials*, 7(5):1601879, 2017.

[11] Theo Christiaanse and Ekkes Brück. Proof-of-concept static thermomagnetic generator experimental device. *Metallurgical and Materials Transactions E*, 1(1):36–40, Mar 2014.

[12] Anja Waske, Daniel Dzekan, Kai Sellschopp, Dietmar Berger, Alexander Stork, Kornelius Nielsch, and Sebastian Fähler. Energy harvesting near room temperature using a thermomagnetic generator with a pretzel-like magnetic flux topology. *Nature Energy*, 4(1):68–74, Jan 2019.

[13] Smail Ahmim, Morgan Almanza, Vincent Loyau, Frédéric Mazaleyrat, Alexandre Pasko, Fabien Parrain, and Martino LoBue. Self-oscillation and heat management in a lafesi based thermomagnetic generator. *Journal of Magnetism and Magnetic Materials*, 540:168428, 2021.

[14] Nikola Tesla. Thermo-magnetic motor, U.S. patent 396121A (1889).

[15] Thomas Alva Edison. Pyromagnetic motor, U.S. patent 380100A (1888).

[16] Tino Gottschall, Konstantin P. Skokov, Maximilian Fries, Andreas Taubel, Iliya Radulov, Franziska Scheibel, Dimitri Benke, Stefan Riegg, and Oliver Gutfleisch. Making a cool choice: The materials library of magnetic refrigeration. *Advanced Energy Materials*, 9(34):1901322, 2019.

[17] V. Franco, J.S. Blázquez, J.J. Ipus, J.Y. Law, L.M. Moreno-Ramírez, and A. Conde. Magnetocaloric effect: From materials research to refrigeration devices. *Progress in Materials Science*, 93:112–232, 2018.

[18] Debabrata Mishra, Mallikarjuna Gurram, Anvesh Reddy, A. Perumal, P. Saravanan, and A. Srinivasan. Enhanced soft magnetic properties and magnetocaloric effect in b substituted amorphous fe–zr alloy ribbons. *Materials Science and Engineering: B*, 175(3):253–260, 2010.

[19] Greta Cavazzini, Francesco Cugini, Davide Delmonte, Giovanna Trevisi, Lucia Nasi, Semih Ener, David Koch, Lara Righi, Massimo Solzi, Oliver Gutfleisch, and Franca Albertini. Multifunctional ni-mn-ga and ni-mn-cu-ga heusler particles towards the nanoscale by ball-milling technique. *Journal of Alloys and Compounds*, 872:159747, 2021.

[20] Francesco Cugini, Lara Righi, Lambert van Eijck, Ekkes Brück, and Massimo Solzi. Cold working consequence on the magnetocaloric effect of ni50mn34in16 heusler alloy. *Journal of Alloys and Compounds*, 749:211–216, 2018.

[21] Xinmin You, Michael Maschek, Niels Harmen H. van Dijk, and Ekkes Brück. Magnetic phase diagram of the mnxfe2-xp1-ysiy system. *Entropy*, 24(1), 2022.

[22] Juan Rodríguez-Carvajal. Recent advances in magnetic structure determination by neutron powder diffraction. *Physica B: Condensed Matter*, 192(1):55–69, 1993.

[23] H. M. Rietveld. A profile refinement method for nuclear and magnetic structures. *Journal of Applied Crystallography*, 2(2):65–71, Jun 1969.

[24] Hamutu Ojiyed, Maarten van den Berg, Ivan Batashev, Qi Shen, Niels van Dijk, and Ekkes Brück. Magnetocaloric properties of mn5(si,p)b2 compounds for energy harvesting applications. *Journal of Alloys and Compounds*, 978:173485, 2024.

[25] G. Cavazzini, F. Cugini, M.E. Gruner, C. Bennati, L. Righi, S. Fabbrici, F. Albertini, and M. Solzi. Tuning the magnetic and magnetocaloric properties of austenitic ni-mn-(in,sn) heuslers. *Scripta Materialia*, 170:48–51, 2019.

[26] Simone Fabbrici, Francesco Cugini, Fabio Orlandi, Nicola Sarzi Amadè, Francesca Casoli, Davide Calestani, Riccardo Cabassi, Greta Cavazzini, Lara Righi, Massimo Solzi, and Franca Albertini. Magnetocaloric properties at the austenitic curie transition in cu and fe substituted ni-mn-in heusler compounds. *Journal of Alloys and Compounds*, 899:163249, 2022.

[27] G. Cavazzini. *Multifunctional Ni-Mn-based Heusler compounds from bulk to nanoparticles by ball-milling techniques*. PhD thesis, Università degli Studi di Parma, Dipartimento di Scienze chimiche, della vita e della sostenibilità ambientale, 2021.

[28] Tanja Graf, Claudia Felser, and Stuart S.P. Parkin. Simple rules for the understanding of heusler compounds. *Progress in Solid State Chemistry*, 39(1):1–50, 2011.

[29] Aslı Çakır, Lara Righi, Franca Albertini, Mehmet Acet, and Michael Farle. Intermartensitic transitions and phase stability in ni50mn50-xsnx heusler alloys. *Acta Materialia*, 99:140–149, 2015.

[30] Thorsten Krenke, Mehmet Acet, Eberhard F. Wassermann, Xavier Moya, Lluís Mañosa, and Antoni Planes. Martensitic transitions and

the nature of ferromagnetism in the austenitic and martensitic states of Ni − Mn − Sn alloys. *Phys. Rev. B*, 72:014412, Jul 2005.

[31] H.A. Toliyat and G.B. Kliman. *Handbook of electric motors: Second edition, revised and expanded*. Marcel Dekker, 01 2004.